


Signatures of spectral crossovers in the short- and long-range spectral correlations of a disordered spin-chain with Kramers degeneracy

Debojyoti Kundu¹,* Santosh Kumar¹,† and Subhra Sen Gupta¹‡*Department of Physics, Shiv Nadar Institution of Eminence (SNIOE), Gautam Buddha Nagar, Uttar Pradesh 201314, India*
 (Received 15 November 2022; revised 9 February 2023; accepted 17 February 2023; published 20 March 2023)

We investigate several distinct spectral crossovers amongst various integrable (Poissonian) and quantum-chaotic (Wigner-Dyson) limits of a 1D disordered quantum spin ($S = 1/2$) model, by tuning the relative amplitudes of various Hamiltonian parameters to retain or break relevant unitary and antiunitary symmetries. The spin model consists of an isotropic and deterministic Heisenberg term, a random Ising term, an anisotropic and antisymmetric, but deterministic Dzyaloshinskii-Moriya (DM) term, and a Zeeman coupling to a random, inhomogeneous magnetic field. Since we are specially interested in crossovers involving a Gaussian symplectic ensemble (GSE) limit, we carry out all our calculations with an odd number of lattice sites (spins) that naturally results in eigenspectra with Kramers degeneracies (KD's). The various crossovers (viz., the reentrant Poissonian-to-GSE-to-Poissonian, Poissonian-to-GUE, GSE-to-GUE and the reentrant Poissonian-to-GOE-to-Poissonian crossovers) are investigated via detailed studies of both short-range (nearest-neighbour-spacings distribution, NNSD) and long-range [spectral rigidity $\Delta_3(L)$ and number variance $\Sigma^2(L)$] spectral correlations, where L is the *spectral interval* over which the long-range statistic is examined. The short-range studies show excellent agreement with RMT predictions. One of the highlights of this study is the systematic investigation of the consequences of retaining both eigenvalues corresponding to every Kramers doublet, in a crossover involving the GSE limit, and see how it evolves to a limit where the KD is naturally lifted. This is seen most clearly in the NNSD study of the GSE-to-GUE (Gaussian unitary ensemble) transition, achieved by gradually lifting the KD, using the random magnetic field. The NNSD plot in the GSE limit here exhibits a Dirac delta peak at zero splitting and a renormalized GSE hump at finite splitting, whose general analytical form and its asymptotic limit are derived. With an increasing symmetry breaking magnetic field the NNSD shows an interesting, dynamic two-peaked structure that finally converges to the standard GUE lineshape. We explain this trend in terms of a competition between the splittings amongst distinct Kramers doublets (related to unitary symmetries) and the Zeeman-like splittings induced by a breaking of the antiunitary time-reversal symmetry (TRS). This is investigated via the NNSD, the marginal spectral density (MSD) and the densities of states (DOS) for both spin models and RMT crossover matrix models. The first and the final short-range studies involve reentrant Poissonian-to-GOE(GSE)-to-Poissonian crossovers, where the final Poissonian is obtained by a many-body localization of states in the strongly disordered limit, whereas the initial Poissonian regime involve much more delocalized eigenstates. In the long-range spectral correlation studies, we shed light on the extent of agreement between our physical spin systems and RMT predictions. We find that the spin systems depart from the ideal RMT predictions for relatively finite $L \sim 10 - 15$ at least, for the *spectral rigidity* and a much smaller $L \sim 2 - 4$ for the *number variance*. It is further seen that the departure is usually sooner at the uncorrelated (Poissonian) upper end compared to the correlated (Wigner-Dyson) lower end. We carry out a detailed comparison between the *local* and the *global* crossover points, associated with the short-range and the long-range statistics respectively, and find that in most cases they seem to agree reasonably well, but for a few exceptions. Our studies also show that the long-range correlations may serve to distinguish between the two Poissonian limits (*nonlocalized* and *localized*) in the reentrant crossovers, which the short-range correlations fail to distinguish.

DOI: [10.1103/PhysRevB.107.094205](https://doi.org/10.1103/PhysRevB.107.094205)

I. INTRODUCTION

The microscopic many-body quantum interactions in a solid are very complex, due to presence of strongly correlated electrons and ions. It is quite impossible to exactly solve the dynamics of such complex systems, but one can certainly gain some insights through some relatively simplified

models, such as the Hubbard models and its generalizations [1–5], obtained after several levels of simplifying assumptions, starting with the Born-Oppenheimer approximation that effectively integrates out the lattice degrees of freedom leading to purely electronic Hamiltonians. In the presence of large on-site Coulomb and exchange interactions, the intersite charge fluctuations and the intrasite orbital and spin fluctuations become irrelevant and these fermionic models can be further reduced to a variety of *spin-only* Hamiltonians. The *isotropic Heisenberg model*, the *XX model*, the *XY model*, the *anisotropic XXZ* and *XYZ models*, the *Ising model*, etc.

*debojyoti.kundu.physics@gmail.com

†Corresponding author: skumar.physics@gmail.com

‡Corresponding author: subhro.sengupta@gmail.com

[6–11], are among the most common ones. Even after so many levels of simplification; most of these interacting spin-models cannot be solved analytically for exact solutions, in arbitrary dimensions. The presence of spin-orbit coupling or magnetic field induced anisotropies further complicate the situation, by introducing terms like the two-spin anisotropic Dzyaloshinskii-Moriya (DM) exchange interaction, or the three-spin scalar-spin-chiral interaction, that leads to even richer phase diagrams with exotic spin phases [12–18]. So one resorts to numerical solutions.

The presence of disorder in solids can further increase the complexity of correlated electron systems. Anderson and coworkers addressed the physics of real (amorphous) solids with impurities but in the absence of interactions [19–23]. But only limited success has been achieved while dealing with the generic disorder problem in correlated electron systems [24–27]. Coming back to spin Hamiltonians, it is encouraging to note that in 1D, several of the above models are integrable and often lead to exact solutions. However, this integrability and related predictability via analytical solutions quickly fades away as soon as disorder is introduced, either in form of site or bond disorder, or via coupling to an inhomogeneous and stochastic external magnetic field [28–30]. Owing to the complexity of correlated electronic and spin systems and unavailability of exact solutions, one seeks some statistical techniques, which can capture some crucial features of the eigenspectra. In this regard, random matrix theory (RMT) naturally appears as a powerful formalism. Originally introduced in the context of studying neutron scattering spectra from heavy nuclei [31–39], it has gradually found its place in the investigation of spectral properties of large complex atoms, molecules, quantum chaotic systems, quantum many-body systems with disorder, quantum dots [39–47], etc. RMT is used to model the relevant operators in a given problem exhibiting complexity and, *inter alia*, can predict universal features of the associated spectra.

Disorder in physical systems in general, and in quantum spin models, in particular, results in a transition to a nonintegrable regime, the spectral statistics of the corresponding Hamiltonians being linked to the three canonical ensembles (GOE, GUE, and GSE) of RMT via the Bohigas, Giannoni, and Schmit (BGS) conjecture [48], as summarized succinctly in the next section. In contrast, the spectral statistics of the former Integrable Hamiltonians are well described by Poissonian statistics, *a la* the Berry-Tabor conjecture [49]. The various physical symmetries of the Hamiltonians are intimately related to the RMT (Wigner-Dyson) spectral classes mentioned above, which is detailed in the next section for ready reference. Even though most of these nonintegrable quantum spin Hamiltonians have no classically chaotic counterpart, the very emergence of Wigner-Dyson spectral statistics is now well accepted to be the quantum signatures of chaos, and consequently these are often referred to as the quantum-chaotic regime. Researchers have examined both short-range [28–30, 47, 50–53] and long-range [54–58] spectral fluctuation behavior of spectra of physical systems using various spectral measures to assess the extent of agreement with RMT and to unveil integrability or nonintegrability aspects.

In our previous paper [28], we considered a Heisenberg spin-1/2 chain in the presence of a Zeeman coupling to a

spatially inhomogeneous and random magnetic field and a scalar spin-chirality term. Our main focus there was to explore the short-range (nearest-neighbor-spacing distribution [NNSD] and ratio distribution [RD]) spectral properties of the above spin-chain and spectral crossovers amongst the integrable (Poissonian) and two Wigner-Dyson ensembles (GOE and GUE). In the present paper, we consider a spin-1/2 quantum spin-chain model involving an isotropic nearest-neighbor Heisenberg coupling, in the simultaneous presence of random Ising interactions, antisymmetric DM interactions, and Zeeman coupled to a random, inhomogeneous magnetic field (details in Sec. III). By tuning the relative amplitudes of the various terms in this complex Hamiltonian, we realize a plethora of RMT spectral crossovers, as detailed later and summarized in Table III (see below). These crossovers are examined via the studies of both short-range (NNSD) as well as long-range [spectral rigidity $\Delta_3(L)$ and number variance $\Sigma^2(L)$] spectral correlations. In the process we also carry out a comparison between the level of correspondence between the short-range correlation dictated *local* and the long-range correlation dictated *global* crossover points.

A highlight of this paper is a detailed study of some crossovers involving the GSE regime *retaining the inherent Kramers degeneracy (KD)* due to an odd number of lattice sites hosting an odd number of spin-1/2's.¹ This is in contrast to more conventional studies where the KD is artificially removed before studying the spectral statistics. This gives rise, for example in the GSE-to-GUE crossover NNSD, to a dynamic double-peak structure in the crossover regime, which we analyze in detail in terms of the marginal spectral density (MSD) as well as the full densities of states (DOS) in the context of both spin Hamiltonians as well as RMT matrix models. In the GSE limit, we also present a derivation of an analytical expression for the NNSD in the presence of KD, dubbed as the modified or diluted GSE distribution. This will also be seen to manifest in the long-range studies in terms of a reduced spectral correlation, not only with respect to the standard GSE, but also the standard GUE.

Moreover, in the course of our studies, we have examined two cases of *reentrant* transitions in the form of the Poissonian-GSE-Poissonian and the Poissonian-GOE-Poissonian crossovers, both of which exhibit two distinct Poissonian regimes. In either case we encounter, in the beginning, a Poissonian regime where several eigenstates are fairly delocalized and end with a Poissonian regime where the eigenstates are strongly localized due to a very strong Ising anisotropy. Although these distinct Poissonian regimes are not distinguishable via the NNSD studies, we demonstrate that they may be distinguished via their long-range spectral fluctuations.

The rest of the paper is organized as follows. In Sec. II, we discuss various spatiotemporal symmetries of the physical Hamiltonians that are required for them to belong to a specific symmetry class. Next, in Sec. III, we describe the spin-chain Hamiltonian used in this study and its various competing

¹An even number of lattice sites hosting an even number of spin-1/2's does not give rise to the desired Kramers degenerate situation, essential for observing the GSE distribution; see e.g., Ref. [28].

TABLE I. Conditions under which a quantum system (e.g., the spin-chain model in our case) achieves different RMT symmetry classes, mathematical nature of the corresponding Hamiltonian matrices, along with the information about integrability of the system. Here the antiunitary operator \mathcal{T} represents the generic antiunitary time-reversal symmetry operator ($T_0 = e^{i\pi S^z/\hbar} K$, or $T = e^{i\pi S^x/\hbar} T_0$), and the unitary operator R_α represents the general spatial (or parity) symmetry (e.g., $R_\alpha = e^{i\pi \mathcal{J}^\alpha/\hbar}$, $\alpha = x$ or y). KD stands for *Kramers degeneracy*, N_s is the number of spin- $\frac{1}{2}$'s in the system.

Mathematical nature of the Hamiltonian matrix	Physical symmetry (and other) requirements	Symmetry class	Integrability of the system
I. Any diagonalizable [random or nonrandom (see second column)]	No specific symmetry requirements 1. No disorder or randomness; OR 2. Localized states with large diagonal disorder (and no or small off-diagonal correlations)	Poissonian ($\beta = 0$)	Integrable
II. Real-symmetric (usually random with finite off-diagonal correlations)	1. $[H, \mathcal{T}] = 0$, $\mathcal{T}^2 = +1$ (No KD present; N_s even) and no specific spatial symmetry requirements; OR 2. $[H, \mathcal{T}] = 0$, $\mathcal{T}^2 = -1$ (KD present; N_s odd), and at least <i>two</i> spatial symmetries (R_α , $\alpha = 1, 2$), along with the conditions: $[H, R_\alpha] = 0 = [\mathcal{T}, R_\alpha]$, $R_\alpha^2 = -1$, $\{R_1, R_2\} = 0$ (anticommutation)	GOE ($\beta = 1$)	Nonintegrable (quantum-chaotic)
III. Complex-Hermitian (usually random with finite off-diagonal correlations)	1. $[H, \mathcal{T}] \neq 0$ (N_s even or odd) and no specific spatial symmetry requirements; OR 2. $[H, \mathcal{T}] = 0$, $\mathcal{T}^2 = -1$ (KD present; N_s odd), and <i>one</i> spatial symmetry (R_α), along with the conditions: $[H, R_\alpha] = 0 = [\mathcal{T}, R_\alpha]$, $R_\alpha^2 = -1$	GUE ($\beta = 2$)	Nonintegrable (quantum-chaotic)
IV. Quaternionic self-dual (usually random with finite off-diagonal correlations)	$[H, \mathcal{T}] = 0$, $\mathcal{T}^2 = -1$ (KD present; N_s odd), <i>no</i> spatial symmetries	GSE ($\beta = 4$)	Nonintegrable (quantum-chaotic)

terms, and the various unitary or antiunitary symmetries that they individually preserve or violate, and how their joint action classifies the full Hamiltonian into one Wigner-Dyson class or another. In Sec. IV, we review various RMT key concepts, like the short-range and long-range spectral correlation properties, and summarize the analytical RMT results used in our analysis. Next, in Sec. V, we present the details of our calculations and showcase the results. It also includes the analysis and discussions of our results. We summarize our findings in Sec. VI. Details of some of the derivations etc. are presented in four separate appendices.

II. CLASSIFICATION OF A HAMILTONIAN INTO INTEGRABLE AND NONINTEGRABLE CLASSES: SPATIOTEMPORAL SYMMETRY REQUIREMENTS

In this short section, we summarize the various physical symmetry requirements on a physical Hamiltonian, in order for its short-range and long-range spectral statistics to be classified as that of an integrable (Poissonian) or nonintegrable/quantum-chaotic (Wigner-Dyson classes) system. Physical symmetries are usually classified as the

more common unitary class (e.g., rotations, parity, translations, time translations, etc.) or the more exotic antiunitary class (time-reversal symmetries, complex conjugation symmetry, particle-hole or charge conjugation symmetry etc.) [38,39,41,59,60]. For our purposes in this paper, we will limit ourselves to various rotation operations as relevant unitary symmetries and *conventional* and *unconventional* time-reversal operations as relevant antiunitary symmetries, as shown in Table I. As also seen from Table I, this limits us to the Integrable (Poissonian) and the three classic Wigner-Dyson classes (GOE, GUE, GSE). This has been mainly compiled on the basis of the Refs. [39] and [41].

The spatial symmetries relevant in this context are represented by the unitary operators $R_\alpha = e^{i\pi \mathcal{J}^\alpha/\hbar}$ ($\alpha = x, y$), where \mathcal{J}^α is the α th component of the relevant angular momentum of the system under consideration. R_α is seen to be the rotation operator about the $\hat{\alpha}$ axis by an angle π , and for this reason it is referred to as a *parity* operator in some references [41]. For a spin- $\frac{1}{2}$ system with no other spatial degrees of freedom, the generator of rotations about the axis $\hat{\alpha}$ is the *Pauli* operator $\sigma^\alpha = \boldsymbol{\sigma} \cdot \hat{\alpha}$ related to the spin operator via $S^\alpha = \frac{\hbar}{2} \sigma^\alpha$.

TABLE II. Invariance of the different Hamiltonian terms under various unitary and antiunitary symmetry operations, and the conserved \mathbf{S} component. Here $\mathcal{R}(\hat{e}, \theta) = e^{i\theta \mathcal{J} \cdot \hat{e}/\hbar}$ represents the general rotation operator about an axis \hat{e} and by an angle θ , generated by the relevant angular momentum operator \mathcal{J} .

Hamiltonian term	T_0	T	$\mathcal{R}(\hat{e}, \theta)$	Rotational invariance axis	Conserved \mathbf{S} component
H_h	✓	✓	✓	Any axis	S^z
H_{ir}	✓	✓	✓	z axis and π rotation about any \hat{e} in xy plane	S^z
H_r	×	✓	✓	z axis	S^z
H_{DM}	✓	×	✓	\hat{D} axis	$\mathbf{S} \cdot \hat{D}$

The *conventional* time-reversal symmetry operator is defined by the usual relation $T_0 = e^{i\pi S^y/\hbar} K$, whereas the *unconventional* time-reversal symmetry operator is given by $T = e^{i\pi S^x/\hbar} T_0$ [29,30,41], where $S^y(S^x)$ is the $y(x)$ component of the spin operator and K is the *complex conjugation operator*, with the property $K^2 = 1$. Acting on a spin \mathbf{S} , T_0 reverses the sign of *all* its components, while T reverses the sign of only the x component. For a system of spin- $\frac{1}{2}$ particles, $T_0^2 = +1$ for an *even* number of spins, and $T_0^2 = -1$ for an *odd* number of spins. On the other hand, $T^2 = +1$ irrespective of the number of spins involved.

It is reasonably well established by now, based on the *Berry-Tabor conjecture* [49], that for *integrable* systems the eigenvalue fluctuation statistics follow the Poissonian distribution in the sense that its eigenvalues seem to behave like a sequence of uncorrelated random variables, with no level repulsion. This is usually associated with the Dyson index $\beta = 0$. This seems to be true for many physical Hamiltonians without disorder but also effectively true for Hamiltonians with large diagonal disorder and relatively negligible off-diagonal elements correlating them (for example, in Ref. [28], the purely Heisenberg case or the high magnetic field case, respectively). On the other hand, the Bohigas, Giannoni, and Schmit (BGS) conjecture [48] seems to ensure that the emergence of Wigner-Dyson statistics (with the degree of level-repulsion, signified by the Dyson index $\beta = 1, 2$, and 4 respectively, for the GOE, GUE, and GSE distributions) for level spacings is a hallmark of *nonintegrable* or *quantum-chaotic* systems, even for many-body quantum Hamiltonians, which do not have a classically chaotic counterpart. The spin-chain Hamiltonian used in our study and its various limits, which give rise to distinct symmetry classes, are described in the following section.

III. METHODOLOGY: THE SPIN HAMILTONIAN, ITS SYMMETRIES, AND CHOICE OF BASIS

Our one-dimensional spin Hamiltonian H has N lattice sites with one spin- $\frac{1}{2}$ per site, and is given by

$$\begin{aligned}
 H &= H_h + H_{ir} + H_r + H_{DM} \\
 &= \sum_{j=1}^{N-1} J \mathbf{S}_j \cdot \mathbf{S}_{j+1} + \sum_{j=1}^{N-1} J \epsilon_j S_j^z S_{j+1}^z \\
 &\quad + \sum_{j=1}^N h_j S_j^z + \sum_{j=1}^{N-1} \mathbf{D} \cdot [\mathbf{S}_j \times \mathbf{S}_{j+1}]. \quad (1)
 \end{aligned}$$

This spin-chain Hamiltonian consists of four terms. The *first* term H_h is the usual isotropic spin- $\frac{1}{2}$ *Heisenberg* term, where \mathbf{S}_j is the spin operator at site j (and S_j^z its z component), with J as the nearest-neighbor-exchange interaction. The *second* term H_{ir} is a random *Ising* term, where the exchange interaction is randomized by multiplying J with the dimensionless random parameter ϵ_j , which follows a Gaussian distribution having zero mean and variance ϵ^2 . The *third* term H_r couples the spin system to a spatially inhomogeneous and random magnetic field. The parameters h_j characterizing the random, inhomogeneous site magnetic fields, follow a Gaussian distribution, having zero mean and variance h^2 [28–30]. The *fourth* term H_{DM} is the antisymmetric *Dzyaloshinskii-Moriya* (DM) interaction [12–14,61,62]. H_{DM} describes the anisotropic effective spin-spin coupling between neighboring spins, induced in second-order perturbation theory via the on-site spin-orbit coupling terms and the intrasite exchange interaction between the relevant sites, after integrating out the orbital degrees of freedom, while retaining spin as an operator. The vector coupling constant \mathbf{D} in H_{DM} carries the orbital contribution and the intersite exchange interaction, while the rest is the antisymmetric spin part ($\mathbf{S}_j \times \mathbf{S}_{j+1}$). This often leads to *canted spin arrangements* [63] in real materials, while competing with the Heisenberg term. A detailed expansion of this term in terms of the site (S_j^z, S_j^+, S_j^-) operators is given in Appendix A, for ready reference.

As already pointed out in the Introduction, the eigenvalue fluctuation statistics of the quantum systems, are guided by the preservation or breaking of various unitary and antiunitary symmetries by the different terms in the Hamiltonian. *Note that for the full Hamiltonian to obey a certain symmetry, all individual terms must abide by it. On the other hand, if even one term violates a certain symmetry, the whole Hamiltonian does not respect that symmetry anymore.* With this in mind, we tabulate in Table II, the invariance/noninvariance of each term of our Hamiltonian with respect to the two antiunitary discrete symmetries T and T_0 , and any possible unitary rotational symmetries, $\mathcal{R}(\hat{e}, \theta) = e^{i\theta \mathcal{J} \cdot \hat{e}/\hbar}$, and the last column summarizes if the total S^z (total z component of spin for the lattice, $S^z = \sum_{j=1}^N S_j^z$) is a conserved quantum number.

Any angular momentum operator \mathcal{J} is odd under the action of the conventional time-reversal symmetry operator, i.e., $T_0 \mathcal{J} T_0^{-1} = -\mathcal{J}$. The spin angular momentum is thus odd under the time-reversal symmetry and the number of spin operators involved in a Hamiltonian term, decides its *evenness* or *oddness* under the T_0 operation. For this reason, H_h , H_{ir} , and H_{DM} are (conventional) time-reversal symmetry invariant ($T_0 H_h T_0^{-1} = H_h$, similarly for H_{ir} and H_{DM}), but H_r is not.

Now, H_h , H_{ir} , and H_r are even and H_{DM} is odd under the *unconventional time-reversal* symmetry, which is represented by the antiunitary operator T . Again, all the Hamiltonian terms other than H_h , break the full rotational invariance (isotropy), but they may be invariant under certain special rotation operations, as elaborated in Table II. However, if different terms of the full Hamiltonian are invariant under rotations about different axes, then in general the Hamiltonian may lack any rotational symmetry at all.

To construct the Hamiltonian in a matrix form, we consider a site-spin direct product basis with a spin- $\frac{1}{2}$ at each lattice site. An up-spin ($m_j^z = \frac{1}{2} \equiv \uparrow$) or a down-spin ($m_j^z = -\frac{1}{2} \equiv \downarrow$) can occupy each of the N lattice sites of the system, where m_j^z is the eigenvalue of S_j^z , so we have 2^N number of basis states $\{|m_1^z m_2^z m_3^z \dots m_N^z\rangle\}$ [28]. From Table II, we notice that the Hamiltonian terms H_h , H_{ir} , and H_r commute with S^z but H_{DM} does not. While for H_h , S^\pm always appear in pairs, H_{ir} and H_r only involve site S^z operators, and hence these three terms can never change the total S^z . On the other hand, as is apparent from Eq. (A4) of Appendix A, which shows the full decomposition of the DM term, only the z component conserves total S^z , while the x and y components are combinations of terms that change the total S^z by ± 1 . Thus, in the absence of the DM term, the different total S^z symmetry sectors are irreducible blocks of the Hamiltonian and hence the eigenvalues between the different sectors are uncorrelated, while only those within a given sector are correlated. On the other hand, the presence of the DM term introduces off-diagonal terms between these irreducible blocks causing all eigenvalues of the full Hamiltonian to become correlated. As a result, in order to observe Wigner-Dyson distributions, we must consider a fixed S^z restricted subspace when $H_{DM} = 0$, while we are *not* permitted to do a similar symmetry adaptation when H_{DM} is finite [39,64], and the *full* basis must be considered. In our calculations with this spin-chain model, we have considered systems where N is *odd*, so that $T^2 = -1$ and Kramers degeneracy is imposed. For simplicity, we keep the $J = 1$ (antiferromagnetic) in our calculations. We need the entire energy spectrum for our spectral correlation studies, so we use the full exact diagonalization methods to obtain the energy eigenvalues. As a result, the system sizes we can access are limited to some extent.

We now explore the conditions under which our spin-chain system achieves different RMT symmetry classes in light of the prior discussions surrounding Tables I and II. In the presence of only the Heisenberg term (H_h) in Eq. (1), the Hamiltonian is preserved under all unitary and antiunitary symmetries, discussed above. Also, there is no disorder in the system, so the fluctuation statistics of the eigenvalues are expected follow the Poissonian distribution. For $H_1 = H_h + H_{ir}$, randomness is introduced in the spin-chain system along z, without breaking either of the time-reversal symmetries. H_1 is also real-symmetric and, as a result of all this, is expected to belong to the Gaussian orthogonal class. If we consider a *fixed S^z subspace*, the fluctuation statistics of the eigenvalues is then expected to follow the GOE distribution. Now, for the *random* Hamiltonian $H_2 (= H_h + H_r + H_{DM})$, both antiunitary symmetries are broken (H_{DM} breaks the T symmetry) and the matrix representation becomes complex-Hermitian [the

DM term induces the complex nature, as is clearly seen from Eq. (A4) of Appendix A, where the x and z components of the DM term are *pure imaginary* and *off-diagonal* and add on to the real terms from the other parts of H_2]. The quantum system represented by H_2 , thus belongs to the Gaussian unitary class. For a *full basis* calculation, the spectral fluctuation statistics is now expected to follow the GUE distribution. Lastly, the *random* Hamiltonian $H_3 (= H_h + H_{ir} + H_{DM})$ preserves the T_0 symmetry (breaks T symmetry due to the H_{DM} term) and breaks all the unitary *spin rotational* (or spatial) symmetries, for the chosen direction of \mathbf{D} . For the system represented by this Hamiltonian, for which conventional time-reversal symmetry is the only remaining symmetry, and with an *odd* number of sites (N) and hence spins, we encounter Kramers degeneracy in the full basis calculation as the only systematic degeneracy left, and the system belongs to the Gaussian symplectic class. The quantum system can then be represented by a quaternionic self-dual matrix and the spectral fluctuation statistics is now expected to follow the GSE distribution. Variations of the relative amplitudes of the various terms in H lead to spectral crossovers amongst the Poissonian and the various Wigner-Dyson distributions. The form of these distributions are tabulated for ready reference in Table IV (see below).

Table III shows the crossover criteria for various symmetry classes in the spin-chain systems (H_1 , H_2 , H_3 , and H). We also list the parameters (in H) that remained fixed during a crossover and those that need to be tuned on in order to break a symmetry and undergo a crossover.

As is customary for random systems, we need to consider the process of *configuration averaging* by diagonalizing an ensemble of \mathcal{M} matrices. Each configuration is a matrix representation of the system with parameters generated at random from Gaussian distributions with fixed widths (standard deviations), h and ϵ [28], respectively, for the two random terms, as relevant. Similar averaging is then repeated for each value of h or ϵ . In Sec. V, we specify the number of configurations used in an ensemble, for each lattice size. Usually, the larger the Hamiltonian matrix dimension, the smaller the number of configurations over which averaging is required to be performed, in agreement with the principle of *spectral ergodicity* [65–67]. While it is customary to remove one of the Kramers degenerate partners from the eigenvalues before studying spectral correlations and obtaining the standard GSE statistics, we also explore spectral correlations retaining the Kramers degeneracies in the spectrum.

IV. RANDOM MATRIX THEORY (RMT)

In this section, we describe the measures of the short-range and long-range spectral correlations in RMT studies used in this paper, and include the RMT analytical results for them. Density of states (DOS) of a physical system is nonuniform, so to compare spectral correlations between different systems, one needs to remove the system-dependent level density from the eigenspectrum, and scale it in terms of the mean level spacing. For this, we need to implement the *unfolding* procedure before comparing our calculated results with the standard RMT results. In our calculations, calculated distribution of states is fitted using polynomials and the fitted polynomial is used to unfold the eigenspectra [28,29,39,41]. For an

TABLE III. Crossovers between various symmetry classes and their criteria (as defined in Table I). Various relevant Hamiltonian parameter values, including the value of the tuning parameter at the NNSD crossover, are also included.

Hamiltonian (N ; basis type)	Crossover from (symmetry criterion from Table I)	Crossover to (symmetry criterion from Table I)	Fixed parameters	Tuning parameter (value at NNSD crossover)
H_3 (13; full basis)	Poissonian (I.1)	GSE (IV)	$J = 1.0; D = 0.2$	ϵ (0.6)
H_3 (13; full basis)	GSE (IV)	Poissonian (I.2)	$J = 1.0; D = 0.2$	ϵ (20.0)
H_2 (13; full basis)	Poissonian (I.1)	GUE (III.1)	$J = 1.0; D = 0.2$	h (0.15)
H (13; full basis)	GSE (IV)	GUE (III.1)	$J = 1.0; \epsilon = 0.6; D = 0.2$	h (0.015)
H_1 (13; $S^z = 1/2$ sector)	Poissonian (I.1)	GOE (II.2)	$J = 1.0$	ϵ (0.5)
H_1 (15; $S^z = 1/2$ sector)	Poissonian (I.1)	GOE (II.2)	$J = 1.0$	ϵ (0.4)
H_1 (13; $S^z = 1/2$ sector)	GOE (II.2)	Poissonian (I.2)	$J = 1.0$	ϵ (20.0)
H_1 (15; $S^z = 1/2$ sector)	GOE (II.2)	Poissonian (I.2)	$J = 1.0$	ϵ (15.0)

ordered sequence $\varepsilon_1 < \dots < \varepsilon_n$, of n energy eigenvalues, the unfolded eigenvalues are calculated using $\tilde{\varepsilon}_j = \int_{\varepsilon_1}^{\varepsilon_j} \rho(\varepsilon') d\varepsilon'$, where $\rho(\varepsilon) = d\mathcal{N}(\varepsilon)/d\varepsilon$ is the fitted DOS, and $\mathcal{N}(\varepsilon)$ is the cumulative DOS (or the *spectral staircase function*).

A. Short-range level correlation statistics

In RMT, it is standard practice to study the short-range level correlations via the nearest-neighbor-spacing distribution (NNSD). It quantifies the local fluctuations of energy eigenvalues of a given system [39,41,44,68]. The nearest-neighbor-level spacing of the unfolded eigenvalues is defined as $s_j = \tilde{\varepsilon}_{j+1} - \tilde{\varepsilon}_j$. The corresponding probability density function $P(s)$ can be compared with the analytical RMT results. The Wigner surmise formulas for the three Dyson symmetry classes along with the Poisson distribution are compiled in Table IV for this purpose.

In this paper, one of our interests is to study the Poissonian-to-GOE, Poissonian-to-GUE, and Poissonian-to-GSE crossovers in NNSD. It is also compelling to study the GSE-to-GUE crossover with and without removing the Kramers degeneracy from the spectra, using the *crossover matrix model* and the spin-chain model. Within RMT, these crossovers can be modeled using the Pandey-Mehta Hamiltonian [69–71]

$$\mathcal{H} = (1 - \alpha)\mathcal{H}_0 + \alpha\mathcal{H}_1, \quad (2)$$

where at $\alpha = 0^2$, the matrix model is governed by the symmetry of \mathcal{H}_0 , and the finite α ($0 < \alpha < 1$) introduces perturbation

²The α in the following expression should not be confused with the component index in Table I and in Sec. II.

TABLE IV. Probability distributions of nearest-neighbor spacings for unfolded eigenvalues [39,41].

Type of distribution	NNSD probability density
Poissonian	$P_{\text{Poi}}(s) = \exp(-s)$
GOE	$P_{\text{GOE}}(s) = (\pi s/2) \exp(-\pi s^2/4)$
GUE	$P_{\text{GUE}}(s) = (32s^2/\pi^2) \exp(-4s^2/\pi)$
GSE	$P_{\text{GSE}}(s) = (2^{18}s^4/3^6\pi^3) \exp(-64s^2/9\pi)$

through \mathcal{H}_1 . At $\alpha = 1$, the other extreme is achieved, where the matrix model is governed by the symmetry of \mathcal{H}_1 . By varying α between 0 and 1, we can study the crossover between two distinct symmetry classes in RMT.

As previously discussed, the Gaussian symplectic class possesses Kramers degeneracy. After removing one of the identical eigenvalues from each of the Kramers doublets, the spectral correlation statistics are usually examined. In this paper, we want to look at the spectral fluctuation for the GSE class *without* eliminating the KD from the eigenspectra. Since, in the absence of any spatial symmetries, we are only left with a series of Kramers doublets, one may guess that this will lead to a GSE-like distribution along with a singular peak at $s = 0$. But in view of this, the whole distribution needs to be renormalized. Below, we present such a modified NNSD formula for an eigenspectrum of n levels, a detailed derivation of which is provided in Appendix C,

$$\mathcal{P}_{\text{GSE}}^n(s) = \left[\frac{2^{12}}{3^6\pi^3} \left(\frac{n-2}{n-1} \right)^6 s^4 \right] \exp \left[-\frac{16}{9\pi} \left(\frac{n-2}{n-1} \right)^2 s^2 \right] + \left(\frac{n}{n-1} \right) \delta(s), \quad (3)$$

where the *Dirac delta* $\delta(s)$ appears because of the presence of KD in the spectra. Since level spacings cannot be negative by definition ($s \geq 0$), we need to consider along with Eq. (3), the definition $\int_0^\infty \delta(s) ds := \frac{1}{2}$. In the large n (number of levels) limit, the Eq. (3) becomes

$$\mathcal{P}_{\text{GSE}}(s) = \left(\frac{2^{12}}{3^6\pi^3} s^4 \right) \exp \left(-\frac{16}{9\pi} s^2 \right) + \delta(s). \quad (4)$$

Starting from GSE, it would be interesting to observe how the initial delta function peak broadens in the NNSD, when one transitions to another symmetry class.

B. Long-range level correlation statistics

As discussed earlier in the Introduction, the long-range eigenvalue fluctuation studies are required to ascertain the extent of universal RMT behavior in a physical system. The two most popular RMT measures to study the long-range spectral properties are the *spectral rigidity* (Δ_3 statistic) and the *number variance* (Σ^2 statistic) [39,41,44,68].

TABLE V. Spectral rigidity (Δ_3 statistic) expressions for the Poissonian and the Wigner-Dyson ensembles, approximated for large L . Here γ is Euler's constant. The full integral expressions (any L) of $\Delta_3(L)$ for the Poissonian and the Wigner-Dyson ensembles can be found in the Appendix D, and are the ones used in our analysis throughout.

Type of ensemble	Spectral rigidity
Poissonian	$[\Delta_3(L)]_{\text{Poi}} = \frac{L}{15}$
GOE	$[\Delta_3(L)]_{\text{GOE}} = \frac{1}{\pi^2}(\ln(2\pi L) + \gamma - \frac{5}{4} - \frac{\pi^2}{8}) + \mathcal{O}(L^{-1})$
GUE	$[\Delta_3(L)]_{\text{GUE}} = \frac{1}{2\pi^2}(\ln(2\pi L) + \gamma - \frac{5}{4}) + \mathcal{O}(L^{-1})$
GSE	$[\Delta_3(L)]_{\text{GSE}} = \frac{1}{4\pi^2}(\ln(4\pi L) + \gamma - \frac{5}{4} + \frac{\pi^2}{8}) + \mathcal{O}(L^{-1})$

For an unfolded eigenspectrum, the *spectral staircase function* $\mathcal{N}(\tilde{\varepsilon})$ denotes the number of levels having energy between 0 and $\tilde{\varepsilon}$. This can be thought of as the cumulative or integrated DOS, $\mathcal{N}(\tilde{\varepsilon}) = \int_0^{\tilde{\varepsilon}} \rho(\tilde{\varepsilon}') d\tilde{\varepsilon}'$. The *least-square* deviation of $\mathcal{N}(\tilde{\varepsilon})$ from the *best fit* straight line ($a\tilde{\varepsilon} + b$, where a and b are obtained from the fit), is defined as the *spectral rigidity* $[\Delta_3(L)]$, for a finite interval L of the eigenspectrum. It is given by the expression

$$\Delta_3(L) = \left\langle \frac{1}{L} \min_{a,b} \left(\int_E^{E+L} [\mathcal{N}(\tilde{\varepsilon}) - a\tilde{\varepsilon} - b]^2 d\tilde{\varepsilon} \right) \right\rangle, \quad (5)$$

where E is the starting position and $\langle \dots \rangle$ denotes the average over several choices of E (*spectral* average) and also over several disordered configurations [39,43,54,59]. The latter *ensemble averaging* over several disordered configurations is performed to mainly obtain statistically smooth data for finite lattice sizes, in our numerical calculations. The analytical RMT formulas for the Poissonian and the Wigner-Dyson ensemble statistics are given in the Table V. These analytical expressions for the Wigner-Dyson ensembles are approximate results in the large L limit. In our studies, we use the full exact integral expressions involving the two-level *cluster functions* [39,59], discussed in the Appendix D.

For the *number variance statistic*, given an unfolded eigenspectrum, one examines the variation in the *number of energy levels* $n(E, L)$ defined as $n(E, L) = \int_E^{E+L} \rho(\tilde{\varepsilon}) d\tilde{\varepsilon}$, in an energy interval of given length L and as a function of the starting energy E . The *number variance statistic* is then defined as [39,43,54,59]

$$\begin{aligned} \Sigma^2(L) &= \langle n(E, L)^2 \rangle - \langle n(E, L) \rangle^2 \\ &= \langle n(E, L)^2 \rangle - L^2, \end{aligned} \quad (6)$$

where the average of $n(E, L)$ becomes L , which is easy to see because the average spectral density for an unfolded spectrum is unity. Here also, as in the case of spectral rigidity, we perform both *spectral* and *ensemble* averages in our relevant numerical calculations. The analytical RMT formulas of $\Sigma^2(L)$ statistic, for the Poissonian and Wigner-Dyson ensembles, are given in the Table VI. See the Appendix D for the full integral expressions involving the two-level *cluster functions* [39,59], which are being used in our studies.

In concluding this section, we also note that the Σ^2 statistic exhibits more fluctuations or oscillations, on the average,

TABLE VI. Number variance (Σ^2 statistic) expressions for the Poissonian and the Wigner-Dyson ensembles, approximated for the large L . Here γ is Euler's constant. The full integral expressions (any L) of $\Sigma^2(L)$ for the Poissonian and the Wigner-Dyson ensembles can be found in the Appendix D, and are the ones used in our analysis throughout.

Type of ensemble	Number variance
Poissonian	$[\Sigma^2(L)]_{\text{Poi}} = L$
GOE	$[\Sigma^2(L)]_{\text{GOE}} = \frac{2}{\pi^2}(\ln(2\pi L) + 1 + \gamma - \frac{\pi^2}{8}) + \mathcal{O}(L^{-1})$
GUE	$[\Sigma^2(L)]_{\text{GUE}} = \frac{1}{\pi^2}(\ln(2\pi L) + 1 + \gamma) + \mathcal{O}(L^{-1})$
GSE	$[\Sigma^2(L)]_{\text{GSE}} = \frac{1}{2\pi^2}(\ln(4\pi L) + 1 + \gamma + \frac{\pi^2}{8}) + \mathcal{O}(L^{-1})$

compared to the Δ_3 statistic. This will also be seen in our studies of the physical spin models. In the context of RMT, this may be understood from the fact that the Δ_3 statistic can be represented as an integral transform involving the Σ^2 statistic [44,68,72], given by the Eq. (D7), leading to the smoother nature of the *spectral rigidity* compared to the *number variance*.

One of the main objectives of this paper is to investigate the correlations between far-off eigenvalues of our spin-chain systems and see how closely they resemble the universal RMT behavior outlined in this section. We further investigate how closely the spectral crossovers, characterized via changes in the short-range and the long-range spectral statistics, correspond with each other.

V. CALCULATIONS AND RESULTS

In this section, we discuss the details of our short- and long-range level correlation calculations, as well as an analysis of the densities of states (DOS) associated with our spin Hamiltonians vis-a-vis RMT matrix models for some of the relevant symmetry crossovers.

A. Nearest-neighbor-spacing distributions (NNSD)

In this section, we report the results from the study of the nearest-neighbor spacings of energy eigenvalues computed from the Hamiltonian H , for an odd number of lattice sites. Here, we consider the lattice size $N = 13$, which has a matrix dimension $n = 8192$ (2^N). We carry out numerical exact-diagonalization calculations with an ensemble size of $\mathcal{M}=15$ configurations, while noting that systems with lattice sizes less than $N = 13$, do not follow the standard RMT ensemble results, closely enough. Also, since the DM term connects the various total S^z sectors (see Appendix A), spin-symmetry adaptation is not feasible in several of these calculations, and the full basis must be used. Hence performing exact-diagonalization calculations for larger lattice sizes having $N = 15$ ($n = 32768$) or more, is computationally very expensive, in view also of the configuration averaging required in all calculations, and so we do not attempt it. As discussed in Sec. III, for odd N , we get *Kramers degeneracy*, i.e., each eigenstate is doubly degenerate, in the case when there is no spatial symmetry left in the system, as in the GSE limit. Here the standard practice is to systematically remove one

of the Kramers degenerate partners by hand before studying the spectral correlation properties of the model. While we have done this, in this paper we have also done calculations retaining the Kramers degeneracy (KD) and compared the results with the standard case where KD has been removed, as discussed below. This often leads to very interesting multi-peak distributions that smoothly evolve from the GSE to other limits where the KD is absent. We consider open boundary conditions (OBC) throughout our calculations, as extra degeneracies might occur in the spectra with periodic boundary conditions (PBC). As mentioned in Sec. IV, we have unfolded the spectra using polynomial fits to make the average level spacing equal to unity.

In Ref. [28], we explored the short-range spectral correlations and crossovers amongst the Poissonian, GOE, and GUE distributions, for an *even* number of sites using a spin-chain model. In this paper, the primary motive behind working with a spin-chain model having an *odd* number of sites, is to achieve the Gaussian symplectic class (GSE) distribution, and study crossovers from/to other distributions in the integrable (Poissonian) or other quantum-chaotic (Wigner-Dyson) limits. To this end we first take up the Poissonian-to-GSE crossover. We tune the relative strengths of the various interactions in the Hamiltonian H_3 to obtain this crossover (see Table III). In the presence of the Heisenberg term (with $J = 1.0$ always, so that all interactions are measured in units of J) and the DM term, and no disorder (randomness) the Poissonian distribution is obtained. To go over to a GSE distribution one needs a complete breaking of any spatial (rotational) symmetry in the system, and this is obtained by the joint action of the H_{ir} and the H_{DM} terms. The H_{ir} term possesses a twofold spin-rotational symmetry about any direction \hat{e} in the xy plane, and reduces the spherical symmetry of H_h to cylindrical symmetry about the z axis, so that only S^z is conserved. H_{DM} alone results in a cylindrical symmetry only about the direction of \hat{D} so that only $\mathbf{S} \cdot \hat{D}$ is conserved (see Table II and Appendix B, for further details). Evidently for any direction of \mathbf{D} distinct from the Ising axis and any axis in the xy plane, there is no rotational symmetry left at all. With this understanding, we make the choice $\mathbf{D} = (D_x, D_y, D_z) = (D, D, D)$. H_{DM} also preserves T_0 (but breaks the T symmetry), which seems sufficient to yield a GSE.

It is however found that *sufficient* breaking of the rotational symmetry of H_h by H_{DM} , to effect a crossover to the GSE distribution, is obtained only at about $D = 0.2$. Hence we fix the magnitude of D at this value at the Poissonian end, and then gradually turn on H_{ir} ($\epsilon = 0 \rightarrow$ finite), which generates *diagonal disorder*, to finally crossover to the GSE distribution at $\epsilon \sim 0.6$. Here we have followed the standard practice of removing one Kramers degenerate partner from each KD. Also the *full basis* has been retained due to the DM term, as discussed earlier. The results of these calculations are shown in Figs. 1(a)–1(d). It compares the results of the spin-chain model (histograms) with the canonical Poissonian and GSE distributions. As seen, fixing $D = 0.2$, we obtain the Poissonian distribution at $\epsilon = 0.0$ [see panel (a)] the pure GSE distribution at $\epsilon = 0.6$ [see panel (d)] and these show an exceptional agreement with the ideal distributions (broken lines). For intermediate values of ϵ , one obtains hybrid distributions, which match with neither limiting distribution,

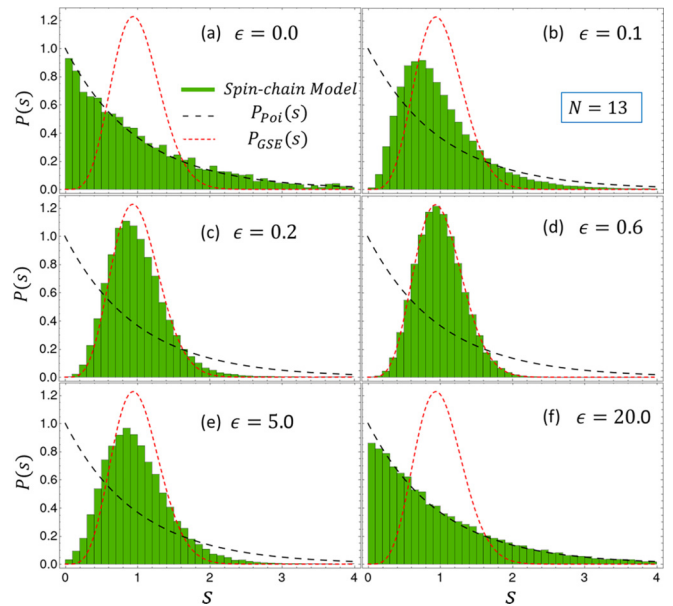


FIG. 1. NNSD for $N = 13$ (basis size $n = 8192$ and the number of configurations $\mathcal{M} = 15$) in the *reentrant* Poissonian-to-GSE-to-Poissonian crossover with increasing ϵ , fixed $D = 0.2$. (a) and (d) show the two limiting cases, namely the Poissonian and the GSE respectively, whereas (b) and (c) show two of the intermediate cases (see also Table III). A further increase of ϵ leads to a reentrant crossover into the Poissonian regime via intermediate stages, as shown in panels (e) and (f). This new Poissonian regime is characterized by a strong many-body localization of its eigenstates, compared to the Poissonian at $\epsilon = 0$.

examples of which are seen in panels (b) and (c). It is to be noted in this context, that in the absence of any time-reversal breaking antiunitary symmetry, the Kramers degeneracy persists throughout this transition. Hence retaining the Kramers doublets, like we do in the GSE-to-GUE transition where TRS is progressively broken, is of no interest here, as it leads to a monotonous singular Dirac delta like peak at $s = 0$ throughout the transition, essentially decoupled from the other peaks. Hence we discard one of the Kramers degenerate eigenvalues systematically before plotting the NNSD. This is in stark contrast to the GSE-to-GUE transition where this Dirac delta like peak moves and merges with the GSE-like peak, also transferring spectral weight in the process, throughout the transition, as will be seen presently.

A further increase of ϵ leads to a reentrant crossover into the Poissonian regime via intermediate distributions that are neither Poissonian nor GSE, a representative case being shown in panel (e) of Fig. 1. In this large ϵ limit the model tends to a random-coupling, nearest-neighbor 1D Ising model (used often to model spin-glasses), where the quantum fluctuations due to the Heisenberg and the DM terms are strongly suppressed by a large uniaxial exchange anisotropy, leading to eigenstates that are many-body localized in this new Poissonian regime. We will again encounter a somewhat similar situation in the context of the Poissonian-to-GOE-to-Poissonian crossover, to be discussed later in the paper.

Next, we study the Poissonian-to-GUE crossover by tuning the relative strengths of the various terms in the Hamiltonian

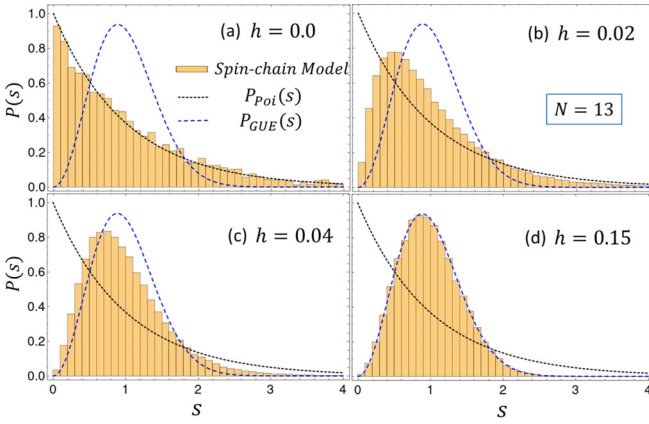


FIG. 2. NNSD for $N = 13$ ($n = 8192$ and $\mathcal{M}=15$) in the Poissonian-to-GUE crossover with increasing h , fixed $D = 0.2$. (a) and (d) show the two limiting cases, namely the Poissonian and the GUE respectively, whereas (b) and (c) show two of the intermediate cases (see also Table III).

H_2 (see Table III). We start again with the nonrandom part of H_2 consisting of H_h and H_{DM} and slowly turn on the random magnetic field (H_r) to crossover into the GUE regime. The details of the parameter values, and criteria used, etc., are summarized in Table III, and the results of our calculations are shown in Fig. 2. When $h = 0$, the level-spacing statistics of the ordered model follows the Poissonian distribution, as shown in Fig. 2(a). Considering the spin-chain model H_2 , at $h = 0.15$ and $D = 0.2$, both conventional and unconventional time-reversal symmetries are now significantly broken (in turn, the KD is lifted), and the NNSD follows the GUE distribution [Fig. 2(d)]. The model H_2 exhibits the Poissonian-to-GUE crossover by varying the random magnetic field h between 0 and 0.15, with D kept fixed at 0.2 (see Table III). While the calculated end members for the spin-chain model (histograms) exhibit excellent agreement with the canonical Poissonian and GUE distributions (broken lines), as seen from Figs. 2(a) and 2(d), the intermediate range hybrid distributions are shown in Figs. 2(b) and 2(c). In the Poissonian limit, one of Kramers degenerate partners is discarded from each Kramers doublet present, as the calculations were carried out using the *full basis*.

Next, *without* removing the Kramers degeneracy from the spectrum, we present an interesting study of the NNSD crossover between the GSE and the GUE distributions, while also comparing the results with the standard case where the KD was removed. As already discussed above, unlike in the Poissonian-to-GSE crossover where the TRS is never broken (and the KD's never lifted), the retaining of the Kramers doublets here, in the GSE-to-GUE crossover, is expected to show an interesting and dynamical evolution of the spectral shape across the crossover. We discuss this in detail now. The information about the parameter values and the basis used are summarized in Table III again. In Figs. 3(a)–3(f), we show the NNSD crossover between the GSE and the GUE distributions for the spin-chain model H (see Table III), by varying the magnetic field h ($D = 0.2$ and $\epsilon = 0.6$ are fixed), which breaks the T_0 symmetry of the system, in the absence of any spatial (rotational) symmetry throughout. In Fig. 3(a),

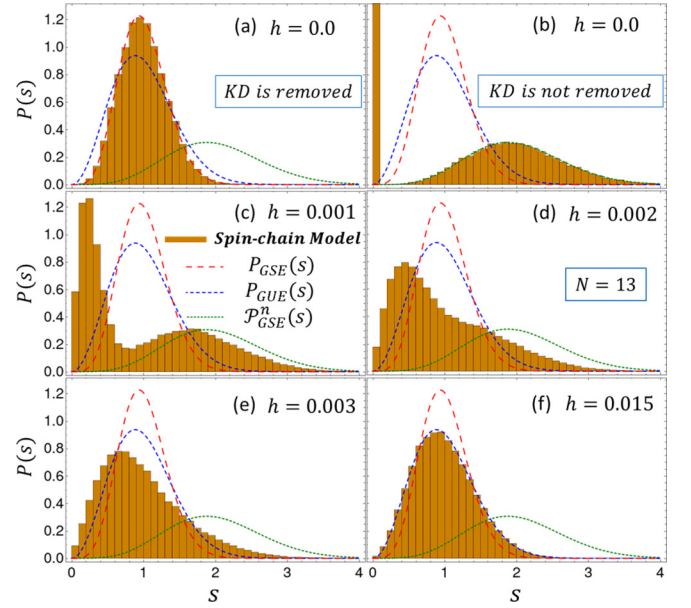


FIG. 3. NNSD for $N = 13$ ($n = 8192$ and $\mathcal{M}=15$). GSE-to-GUE crossover with increasing h , fixed $D = 0.2$ and $\epsilon = 0.6$ (see also Table III). KD is present at $h = 0$. (a) shows the NNSD after removing KD, and it follows $P_{GSE}(s)$, as expected. In (b), the NNSD is plotted without removing KD, which follows the analytical distribution $\mathcal{P}_{GSE}^n(s)$, derived in Appendix C and as predicted by RMT. The agreement is excellent. KD is lifted for finite h , and the NNSD is plotted in (c)–(f). $\mathcal{P}_{GSE}^n(s)$ to $P_{GUE}(s)$ crossover with increasing h is observed. (f) shows the limiting case, which coincides with the NNSD of GUE, at a relatively modest value of $h = 0.015$. An interesting double-peaked structure is observed in the crossover regime, as seen in (c) and (d).

we show the results for the spin-chain model calculations (histogram) and observe that it faithfully follows the standard GSE NNSD [$P_{GSE}(s)$] at $h = 0.0$, where the calculation is carried out after discarding the Kramers degeneracy from the spectrum. However, when KD is not removed from the spectrum [Fig. 3(b)], the NNSD from the spin-chain model follows the derived analytical result $\mathcal{P}_{GSE}^n(s)$ [Eq. (3)]. We can observe the *Dirac delta* peak of $\mathcal{P}_{GSE}^n(s)$ at $s = 0$, which originates from the *zero* spacings between the various Kramers doublets. The nondegenerate eigenvalues generate the broad hump of the modified GSE-like distribution part of $\mathcal{P}_{GSE}^n(s)$, at finite s [$\sim (3/2)\sqrt{\pi/2}$], between the distinct Kramers doublets. The width of this hump at $h = 0$ is contributed partly by the multitude of distinct splittings between various Kramers doublets and also largely by the width of the distribution of the random Ising term ($\epsilon = 0.6$). A detailed derivation of this modified GSE distribution [$\mathcal{P}_{GSE}^n(s)$] retaining the Kramers doublets and for a general n , is presented in Appendix C, and its large n limit is also discussed. As seen, it consists of a Dirac delta peak at $s = 0$ and a broad hump at finite s , which, as we will see, is a variant of the original GSE distribution. As we increase h , the Kramers degeneracy is lifted, and the Dirac delta peak broadens and moves away from $s = 0$. But, the nonzero spacings are now reduced and overall hump at finite s now moves towards a lower value of s . This trend, and related spectral weight transfer, begins to show up in Fig. 3(c) and the two peaks continue to move towards each other in Fig. 3(d),

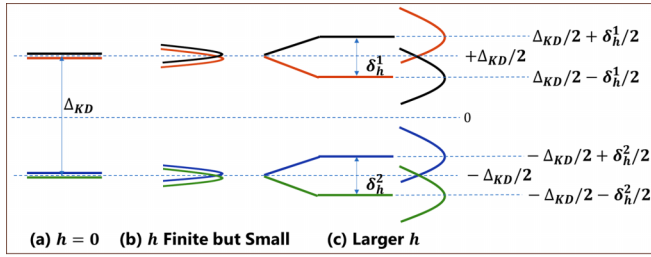


FIG. 4. Evolution of the marginal spectral densities (MSD) and level spacings with increasing h . Panel (a) represents the case for $h = 0$, where the Kramers doublets are truly degenerate, and one has only two distinct level spacings, $s = 0$ and $s = \Delta_{KD}$. The width due to the already present random distribution of the Ising ϵ is ignored here to focus on the dynamics due to h alone. The presence of ϵ will only contribute further to all broadenings, in addition to also broadening the discrete levels in panel (a). In panel (b), h is small but finite and the Kramers doublets split, and the MSD now gain a narrow width, centered about the slightly split Kramers doublets. In panel (c), a larger finite value of h further splits each of the Kramers doublets, but in general by different amounts, δ_h^1 and δ_h^2 . The MSD evolves from a two-peak structure in (b) to a four-peak structure in (c), leading also to three finite nearest-neighbor-level spacings.

before finally merging into a single peak in the GUE limit (at $s \sim \sqrt{\pi}/2$), as from Figs. 3(e) and 3(f). It is also observed that a very small symmetry breaking field, $h = 0.015$, is enough to lead the spin system (H) into the GUE regime, and the NNSD finally achieves the $P_{GUE}(s)$ [Fig. 3(f)].

The understanding of this is especially intuitive within the physical spin model. With the introduction of a finite h , the degeneracy of all the Kramers doublets are simultaneously lifted, due to the breaking of time-reversal symmetry. This Zeeman splitting between the various Kramers doublets now constitute the new peak at a small but finite s that replaces the Dirac delta peak at $s = 0$. It also gains a finite width due to the fact that the Zeeman splitting of the different Kramers doublets are, in general, different depending on the value of S^z that appears in the Kramers doublet (as states with $\pm S^z$, the splitting is proportional to S^z). A second important contribution to the broadening comes from the width of the distribution for the h_j 's themselves, represented by the value of h . Since the center of gravity of the individual Kramers doublets remain intact when the magnetic field splits the Kramers doublets, it is evident that as the Zeeman splittings of the Kramers doublets increase, the nearest-neighbor separation between the *lower* Zeeman-split partner of a certain Kramers doublet and the *upper* Zeeman-split partner of its immediately lower Kramers doublet will reduce. This causes the higher- s hump to move towards a lower- s value in Fig. 3(c), along with a concurrent movement of the Dirac delta derived small- s peak towards higher energies, due to an overall increase in the Zeeman splittings of all Kramers doublets. With a further increase in the magnetic field, the Zeeman splittings between the Kramers doublets further increase, which concurrently reduces the splittings between distinct Kramers doublet split states, and the aforesaid movements of the peaks continue, as seen from Fig. 3(d).

This is also schematically depicted in Fig. 4 for a simplified model with two Kramers doublets, and ignoring the effect of

the finite ϵ for now, remembering that it also contributes to the widths of the various peaks seen in our actual calculations. For $h = 0$, as shown in panel (a), the Kramers doublets are truly degenerate, so that one has two distinct level spacings only, $s = 0$ *within* the two Kramers doublets and a finite $s = \Delta_{KD}$ *between* the pair of Kramers doublets. With the introduction of a small but finite h the Kramers doublets split, but now also gain a width due to the spread in h . This is shown in panel (b) by the narrow and slightly displaced distributions centered about the original discrete levels. With a further increase in h to a larger finite value, each of the Kramers doublets split even more, but in general by different amounts given by the values δ_h^1 and δ_h^2 here, as shown in panel (c). The corresponding widths of the marginal spectral densities (MSD), centered about these states, are also seen to increase as h increases. Now one has four peaks in the MSD, and three different level spacings (s), in general, as seen from Fig. 4. The bare discrete level energies are marked in the figure that yields the values $s = \delta_h^1$, δ_h^2 , and $[\Delta_{KD} - \frac{1}{2}(\delta_h^1 + \delta_h^2)]$ for the three bare level spacings. So even this simple model shows how the MSD may evolve from a two-peak to a four-peak structure, and the NNSD may evolve from a two-peak to a three-peak structure, for example, as h is increased. This further clarifies the origin of the trends seen in our physical spin model, as depicted in Fig. 3 above.

Although the above discussion on the origin of the double-peak structure within the spin-chain model is enlightening, it should not give the reader the impression that the qualitative nature of this behavior is specific to spin models alone. In fact we will show below that this behavior is generic of any GSE-to-GUE crossover, whenever the Kramers degeneracy is retained, rather than weeded out. Although this is already borne out by the analytical calculation for $\mathcal{P}_{GSE}^n(s)$ in the GSE limit, an analytical calculation for the intermediate regime may be a daunting task. The best way to then demonstrate the robustness of this behavior, across the entire crossover, would be to repeat the calculation for a *crossover matrix model* numerically within the Pandey-Mehta approach, which has no direct connection with any specific physical model. To facilitate a reasonably detailed comparison with our calculation, in terms of the shape of the spectral distribution etc., we do this for the exact same matrix dimension as the spin-chain model, viz., $n = 8192$. For the GSE-to-GUE crossover, the *crossover matrix model* of Eq. (2) becomes

$$\mathcal{H} = (1 - \alpha)\mathcal{H}_{GSE} + \alpha\mathcal{H}_{GUE}. \quad (7)$$

We also keep the ensemble size for configuration averaging same as that of the spin model ($\mathcal{M} = 15$). At $\alpha = 0$, the NNSD of the matrix model yields $P_{GSE}(s)$ as expected [Fig. 5(a)], when KD is removed from the spectrum. In the Figs. 5(b)–5(f), the NNSDs are plotted without removing the KD. Similar to the spin-chain model, we again observe the *Dirac delta* peak of $\mathcal{P}_{GSE}^n(s)$ at $s = 0$. The Figs. 5(b)–5(f), represent the NNSD crossover between $\mathcal{P}_{GSE}^n(s)$ to $P_{GUE}(s)$, with increasing α . The intermediate distributions [Figs. 5(c) and 5(d)] also show a similar two-peaked structure as observed for the physical system [Figs. 3(c) and 3(d)]. We observe that the NNSD converges to the GUE distribution at $\alpha = 0.07$, which is rather small compared to the analytical RMT requirement ($\alpha = 1.0$), and seems to track the time-reversal symmetry

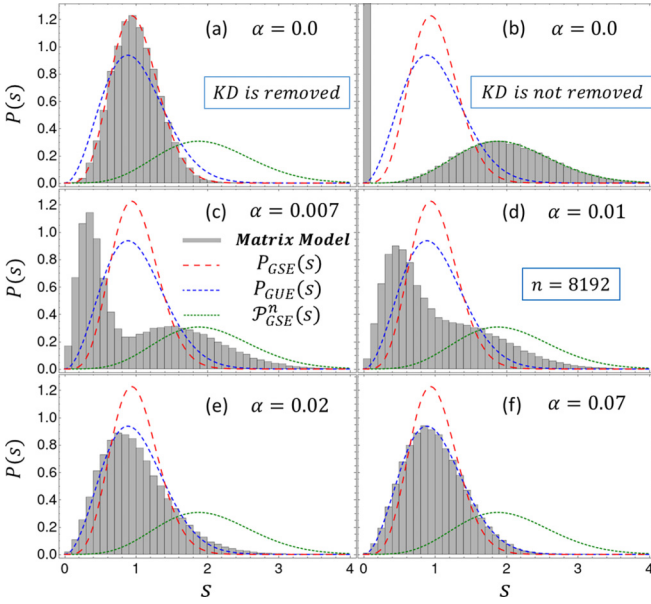


FIG. 5. NNSD of unfolded eigenvalues of the matrix model [Eq. (7)] with $n = 8192$, considering an ensemble of $\mathcal{M} = 15$ matrices, for the GSE-to-GUE crossover. KD is present at $\alpha = 0$. (a) shows NNSD after removing the KD, and it follows $P_{\text{GSE}}(s)$, as expected. In (b), the NNSD is plotted without removing the KD, which follows the analytical RMT distribution $\mathcal{P}_{\text{GSE}}^n(s)$, as derived in Appendix C. KD is lifted for finite α , and the NNSD is plotted in (c)–(f). $\mathcal{P}_{\text{GSE}}^n(s)$ to $P_{\text{GUE}}(s)$ crossover with increasing α is observed. (f) shows the limiting case ($\alpha = 0.07$) where the NNSD matches the GUE distribution. This crossover RMT parameter value of 0.07 is quite small, in agreement with the small value of h required for the physical crossover in Fig. 3. Just as in the spin model, the unusual double-peak structure is seen in the crossover regime, as shown in (c) and (d).

breaking rather faithfully and with minimal lag. It is also consistent with the extremely small magnetic field required in Fig. 3(f), to reach the GUE limit. This behavior is expected from such a large dimensional matrix model, which is consistent with the discussions in Refs. [28,68,69,73,74], regarding the rate of the crossovers with the matrix-dimensions. We conclude from this RMT matrix model study that similar qualitative NNSD crossover behavior between the GSE and the GUE limits should be achieved with any relevant many-body quantum system, provided it satisfies the relevant symmetry requirements as listed in Table I.

Although the large matrix model is useful in establishing the robustness of the double-peak structure and its evolution across the crossover, a smaller matrix model is more transparent in analyzing this behavior and reinforcing our conjecture regarding the origin of this behavior, made in the context of the spin model. Hence, in addition to the NNSD, we also look at the evolution of the MSD across the crossover, in such a model, to see how the states themselves evolve with α . To this end, we consider the crossover matrix model [Eq. (7)] with dimension $n = 4$ and plot (Fig. 6) the MSD of the individual four eigenvalues ($\varepsilon_1, \varepsilon_2, \varepsilon_3$, and ε_4), considering an ensemble of $\mathcal{M} = 20\,000$ matrices. It clearly shows how the Kramers degeneracy is lifted for the GSE-to-GUE crossover with increasing α . In Fig. 6(a), we show MSD of the ma-

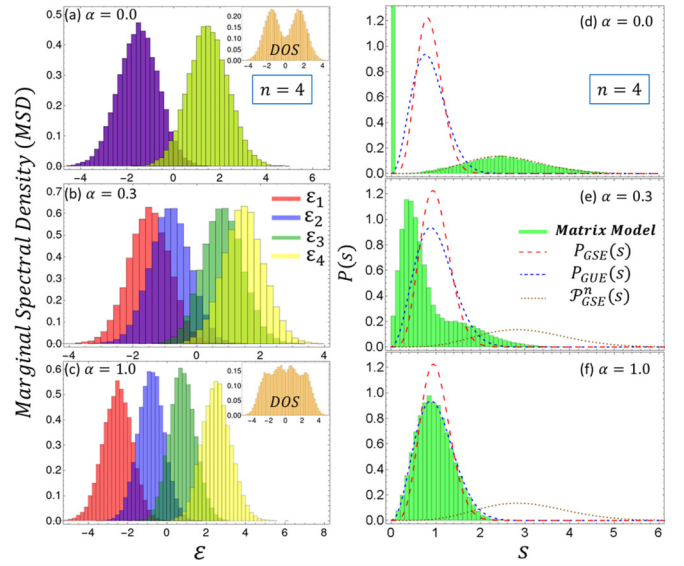


FIG. 6. Marginal spectral density (MSD) of the four individual eigenvalues ($\varepsilon_1, \varepsilon_2, \varepsilon_3$, and ε_4) of the matrix model [Eq. (7)] with $n = 4$ and a configuration of $\mathcal{M} = 20\,000$ matrices. It shows how KD is lifted for the GSE-to-GUE crossover with increasing α . (a) represents the MSD for the GSE matrix model ($\alpha = 0$), which exhibits KD, due to which the MSD of ε_1 and ε_2 (ε_3 and ε_4) are superimposed on one another. At finite α , the splitting between ($\varepsilon_1, \varepsilon_2$) and ($\varepsilon_3, \varepsilon_4$) increases, which can be seen in (b) and (c). (c) shows the limiting case ($\alpha = 1.0$) where the matrix model represents the GUE class, and the splitting is maximum for the eigenvalues. The two insets in (a) and (c) represent the combined DOS of the four eigenvalues, which exhibit interesting two-peak and four-peak structures. (d)–(f) show the corresponding NNSD plots.

trix model in the pure GSE limit ($\alpha = 0$), which exhibits the KD, as a result the distribution of ε_1 and ε_2 (ε_3 and ε_4) are superimposed on one another. With the increase of α the splittings between ($\varepsilon_1, \varepsilon_2$) and ($\varepsilon_3, \varepsilon_4$) increase, which can be seen from the displacements of their MSD peaks, in Figs. 6(b) and 6(c). In Fig. 6(b), the two peaks in Fig. 6(a) have each split into two Kramers partners. The *violet* peak has separated into a *red* and a *blue* one, while the *yellowish-green* peak splits into a *pure green* and a *pure yellow* one. These splittings keep increasing with increasing α . Figure 6(c) shows the limiting case ($\alpha = 1.0$), where the matrix model represents pure GUE, and the separations between the MSD peaks are maximum. The two *insets* in the Figs. 6(a) and 6(c), represent the combined DOS of the four eigenvalues, and show how the original two-peak structure in *inset* of the Fig. 6(a) evolves into a interesting four-peak structure in *inset* of the Fig. 6(c). The above description is well in line with our proposed conjecture above. The corresponding NNSD plots are represented in the Figs. 6(d)–6(f), which are consistent with the higher dimensional behavior as seen both for the spin system [Figs. 3(b)–3(f)] as also for the larger matrix model [Figs. 5(b)–5(f)].

Finally, we consider four individual eigenvalues from a spin-chain calculation and look at the evolution of their MSD with increasing h , to demonstrate explicitly that similar physics is operative as in the $n = 4$ matrix model above. In Figs. 7(a) and 7(b), we present the MSD of the spin-chain

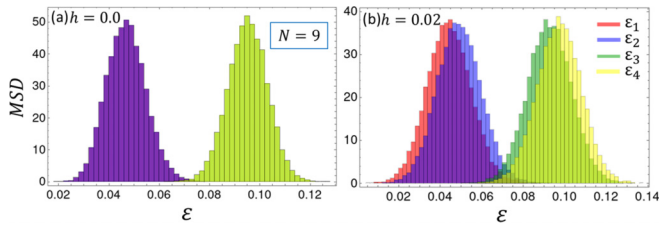


FIG. 7. Marginal spectral density (MSD) of the four individual eigenvalues (ε_1 , ε_2 , ε_3 , and ε_4) (selected from the central peak region of the spectra), of the spin-chain model H with $N = 9$ and a configuration of $\mathcal{M} = 20\,000$ matrices. It shows how the KD is lifted in a physical system for the GSE-to-GUE crossover with increasing symmetry breaking field h (fixed $\varepsilon = 0.6$, $D = 0.2$). (a) represents the case of GSE ($h = 0$), which exhibits the KD, due to which the MSD of ε_1 and ε_2 (ε_3 and ε_4) are superimposed on one another. With an increase of h , the splittings between (ε_1 , ε_2) and (ε_3 , ε_4) increase, and (b) shows the splitting between MSD of the eigenspectrum, in the GUE limit ($h = 0.02$).

model H , with lattice size $N = 9$. We examine two sets of the Kramers degenerate eigenvalues (keeping a separation of 10 eigenvalues) from the middle of the spectra, considering an ensemble of $\mathcal{M} = 20\,000$ configurations, to obtain smooth MSD plots.³ A small magnetic field, $h = 0.02$ (fixed $\varepsilon = 0.6$, $D = 0.2$), is enough to lift the KD and drive the system from the GSE class to the GUE class. Here, in Fig. 7(b), the two peaks in Fig. 7(a) have each split into two Kramers partners and four distinct peaks are observed, similar to what we observe for the matrix model in Figs. 6(a)–6(c).

Now, we are interested to study the Poissonian-GOE-Poissonian (*nonchaotic* \rightarrow *chaotic* \rightarrow *localized* transition) reentrant crossover, in the spin-chain model H_1 . We previously discussed in Sec. III, how the spin-chain model H_1 preserves both (the T_0 and the T) time-reversal symmetries and has a diagonal disorder (random Ising interaction along the z axis). In addition, H_1 possesses full rotational symmetry about the z axis and also has the discrete rotational symmetries (rotation by π) about the x or the y axes (or for any axis in the x – y plane, for that matter), which is in consonance with condition II.2 of Table I. As H_1 commutes with S^z , we need to restrict any calculation for H_1 , to a fixed S^z subspace (see Table III for full details). Here, for an *odd* N , we consider the $S^z = \frac{1}{2}$ subspace ($n = 1716$ for $N = 13$ and $n = 6435$ for $N = 15$ systems), which is the lowest S^z subspace and hence has representations from all possible total S sectors. At $\varepsilon = 0.0$, there is no disorder in the system, and we achieve the Poissonian limit for the NNSD studies [Fig. 8(a) for the $N = 13$ and Fig. 8(d) for the $N = 15$ lattice sizes]. Due to the *self-averaging* or the *spectral ergodicity* property of RMT [28,41,75], we observe much smoother Histogram plots for the $N = 15$ system, compared to the $N = 13$ system. The GOE distribution is achieved at $\varepsilon = 0.5$ [Fig. 8(b)] and $\varepsilon = 0.4$ [Fig. 8(e)], for the $N = 13$ and the $N = 15$ systems, respectively. Further increase of diagonal disorder, results in

³To obtain a smooth MSD of only four individual eigenvalues, we need to consider a large number of configurations, and hence a $N = 13$ calculation is computationally very expensive for this purpose.

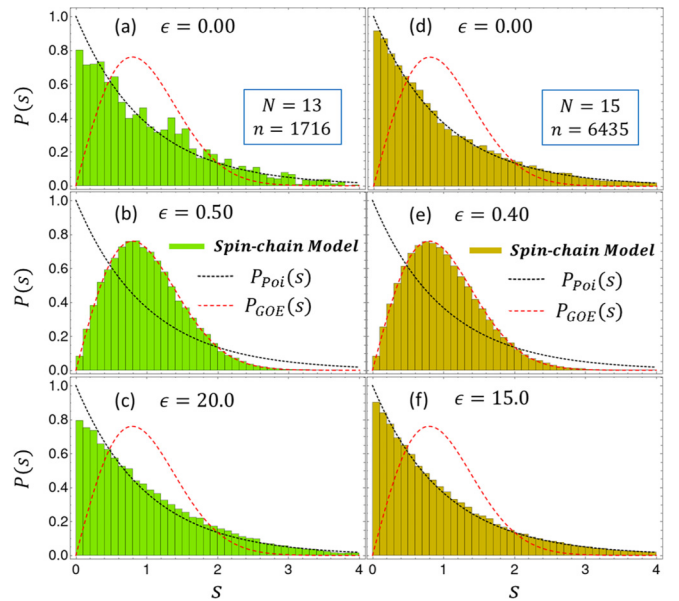


FIG. 8. NNSD for the Poissonian-to-GOE-to-Poissonian reentrant crossovers with increasing ε , within the spin-chain model H_1 , for the lattice sizes $N = 13$ ($\mathcal{M} = 25$) [(a)–(c)] and $N = 15$ ($\mathcal{M} = 15$) [(d)–(f)]. (a) shows that the NNSD follows the Poissonian distribution when ε is zero, (b) shows that the NNSD follows the GOE distribution for $\varepsilon = 0.5$, and (c) shows how Poisson distribution is recovered due to eigenvector localization for a typical large disorder ($\varepsilon = 20.0$). Similarly, for $N = 15$, NNSD is plotted in (d)–(f) for Poissonian-to-GOE-to-Poissonian crossover. One observes that the GOE and the Poissonian in the localized limit are obtained for lower values of ε in the $N = 15$ lattice, compared to the $N = 13$ lattice. Here the localized Poissonian limit is already achieved for $\varepsilon = 15$.

the onset of localization in the eigenstates. This recovers the Poissonian distribution in the strongly disordered limit, viz., $\varepsilon = 20.0$ and $\varepsilon = 15.0$ for the $N = 13$ [Fig. 8(c)] and the $N = 15$ [Fig. 8(f)] systems, respectively. At this stage we should take note of the similarities in the trends and the associated physics, with the reentrant Poissonian-to-GSE-to-Poissonian crossover, discussed at the beginning of this section. This is also strongly reminiscent of a similar Poissonian \rightarrow GOE \rightarrow Poissonian reentrant crossover encountered in our earlier paper [28], where a random inhomogeneous magnetic field term competes with the Heisenberg term to bring about the many-body localization, in the large diagonal disorder limit.

B. Spectral rigidity and number variance

Till now our studies seem to indicate that the short-range eigenvalue correlation statistics of the spin-chain models follow RMT predictions quite accurately. This is also borne out by earlier studies of short-range spectral correlations in other 1D spin models [28–30,61,64]. We now want to study the long-range eigenvalue correlation properties and related spectral crossovers, in our above spin model, in the presence of tunable symmetry-breaking physical parameters. We also compare the values of the symmetry-breaking physical crossover parameters between the short-range (NNSD) and long-range (spectral rigidity and number variance) spectral fluctuation studies. As already mentioned, in Table III,

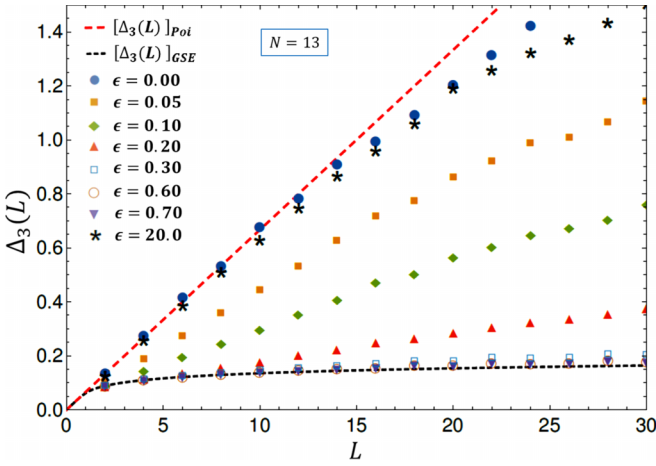


FIG. 9. Spectral rigidity (Δ_3 statistic) for the $N = 13$ spin chain ($\mathcal{M} = 15$) across the Poissonian-to-GSE crossover, with increasing ϵ , and fixed $D = 0.2$ (symbols). For the extremal cases, where one expects the physical system to follow either of the pure statistics (Poissonian or GSE), we have also plotted the RMT exact analytical predictions (broken lines), for comparison. It also shows the Δ_3 statistic for the many-body localized phase, brought about by the large disorder ($\epsilon = 20.0$) (black asterisks), which is again expected to follow the Poissonian result approximately (red broken line).

we have listed the physical crossover parameter values for the NNSD.

Using Eq. (5), we calculate the $\Delta_3(L)$ statistic for the lattice size $N = 13$, in the various possible spectral crossovers listed in Table III, as described below. In Fig. 9, we show the $\Delta_3(L)$ for Poissonian-to-GSE-to-Poissonian reentrant crossover plots with increasing ϵ . This simply introduces randomness without breaking any time-reversal symmetry. Here, we study the long-range correlations amongst eigenvalues with interval length ranging from $L = 2$ to $L = 30$, in steps of 2. In this calculation, one of the Kramers degenerate partners is discarded from each doublet. We observe that $\Delta_3(L)$ follows the analytical Poissonian result $[\Delta_3(L)]_{\text{Poi}}$ up to $L \sim 14$ and then deviates from it. With increasing value of the random parameter ϵ , Poissonian-to-GSE crossover is achieved at $\epsilon = 0.6$ and $\Delta_3(L)$ follows the analytical GSE result $[\Delta_3(L)]_{\text{GSE}}$ quite well, up to large eigenvalue interval lengths. We have earlier achieved the GSE crossover in NNSD at same same value of the random parameter ϵ . Even an increased value of $\epsilon = 0.7$ does not reflect any better agreement, as is evident from the figure. This shows that, at $\epsilon = 0.6$, the eigenvalue fluctuation properties of the spin-chain system (H_3), follow GSE statistics at both the *local* (or short-range) and the *global* (or long-range) scales.

Now, using Eq. (6), we calculate the number variance $\Sigma^2(L)$ for the spin-chain systems with lattice size $N = 13$, considering the eigenvalue interval length starting from $L = 0.5$ to $L = 10$, in steps of 0.5. In Fig. 10, we show the Poissonian-to-GSE-to-Poissonian crossover in $\Sigma^2(L)$ statistic for the spin-chain model H_3 . We observe that, in the absence of the random Ising interaction, $\Sigma^2(L)$ follows the Poissonian analytical prediction $[\Sigma^2(L)]_{\text{Poi}}$ only up to an eigenvalue interval length $L \sim 2$, beyond that it deviates from the ideal result. In the GSE regime ($\epsilon = 0.6$), the $\Sigma^2(L)$ statistic of the spin-

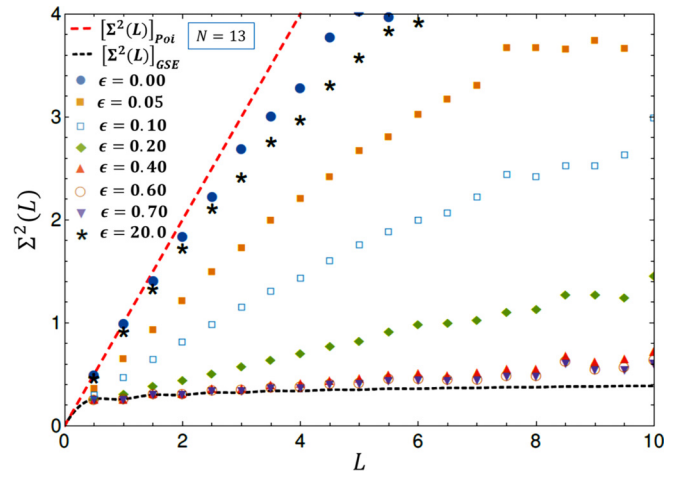


FIG. 10. Number variance (Σ^2 statistic) for the $N = 13$ spin chain ($\mathcal{M} = 15$) across the Poissonian-to-GSE crossover with increasing ϵ , and fixed $D = 0.2$ (symbols). For the extremal cases, where one expects the physical system to follow either of the pure statistics (Poissonian or GSE), we have also plotted the RMT exact analytical predictions (broken lines), for comparison. It also shows the Σ^2 statistic for the many-body localized phase, brought about by the large disorder ($\epsilon = 20.0$) (black asterisks), which is again expected to follow the Poissonian result approximately (red broken line).

chain model almost perfectly overlaps with the oscillatory statistical function $[\Sigma^2(L)]_{\text{GSE}}$ (the oscillatory nature comes from the full integral expressions discussed in the Appendix D), up to an eigenvalue interval length $L \sim 4$, beyond that it deviates. As the figure shows, even an increased value of $\epsilon = 0.7$ does not result in better agreement.

The two Poissonian limits, $\epsilon = 0.0$ and $\epsilon = 20.0$, coincide with the ideal Poissonian result $[\Delta_3(L)]_{\text{Poi}}$ ($[\Sigma^2(L)]_{\text{Poi}}$) (broken red line), till up to $L \sim 14$ and 8 ($L \sim 2$ and 1), respectively. Although both the ordered ($\epsilon = 0.0$) and the highly disordered ($\epsilon = 20.0$) limits tend to agree with the ideal Poissonian prediction till a finite L value, it seems that the disordered/localized Poissonian limit starts to deviate sooner (for a lower L) than the ordered Poissonian limit from the ideal Poissonian result, for both the Δ_3 and the Σ^2 statistics. This seems unlike the short-range correlations [see Fig. 1, especially panels (a) and (f)] where both these limits seem to follow the Poissonian distribution equally faithfully (for similar behavior in a different spin model, see Ref. [28]). *This property of long-range correlations may serve to distinguish between the two different Poissonian regimes, which NNSD is not able to distinguish.*

Now, we study the spectral rigidity of the spin-chain system in model H_2 with $N = 13$. The system undergoes a Poissonian-to-GUE crossover (see Table III) with increasing h , keeping D fixed at 0.2. Figure 11 shows the $\Delta_3(L)$ statistic with interval length starting from $L = 2$ to $L = 30$. We observe that at $h = 0.0$ (KD is present, one of Kramers degenerate partners is discarded from each doublet), $\Delta_3(L)$ statistic coincides with the $[\Delta_3(L)]_{\text{Poi}}$ for L values up to 14, just like for the Poissonian-to-GSE transition, discussed above. At the *local* (or short-range) GUE limit ($h = 0.15$), we notice that $\Delta_3(L)$ statistic follows the standard GUE result

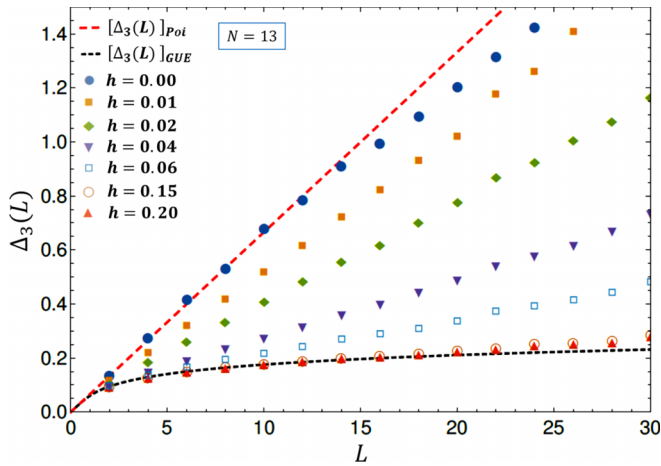


FIG. 11. Spectral rigidity (Δ_3 statistic) for the $N = 13$ spin chain ($\mathcal{M} = 15$) across the Poissonian-to-GUE crossover with increasing h , and fixed $D = 0.2$ (symbols). For the extremal cases, where one expects the physical system to follow either of the pure statistics (Poissonian or GUE), we have also plotted the RMT exact analytical predictions (broken lines), for comparison.

$[\Delta_3(L)]_{\text{GUE}}$ till $L \sim 14$. If we further increase h to 0.2, we do notice some improvement in agreement with $[\Delta_3(L)]_{\text{GUE}}$, up to $L \sim 20$. So, for this case, $h = 0.2$ serves as a better crossover point for the *global* GUE crossover, and $h = 0.15$ can be regarded as a more of a *local* crossover point. We have also plotted the $\Delta_3(L)$ statistic for the intermediate cases in Fig. 11.

In Fig. 12, we plot the level number variance $\Sigma^2(L)$ of the spin-chain model H_2 , having $N = 13$ sites, for the eigenvalue interval length starting from $L = 0.5$ to $L = 10$, in steps of 0.5. We observe that $\Sigma^2(L)$ follows the analytical Poissonian result (at $h = 0.0$) only up to $L \sim 2$, beyond that it deviates from this ideal value, just like in the Poissonian-to-GSE crossover. The Poissonian-to-GUE crossover is achieved

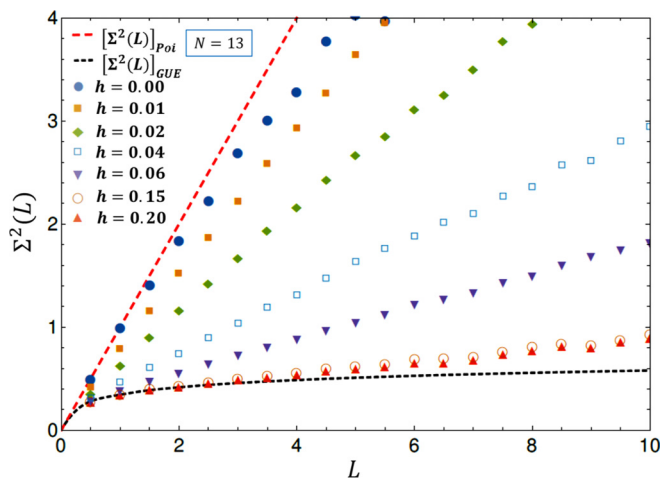


FIG. 12. Number variance (Σ^2 statistic) for the $N = 13$ spin chain ($\mathcal{M} = 15$) across the Poissonian-to-GUE crossover with increasing h , and fixed $D = 0.2$ (symbols). For the extremal cases, where one expects the physical system to follow either of the pure statistics (Poissonian or GUE), we have also plotted the RMT exact analytical predictions (broken lines), for comparison.

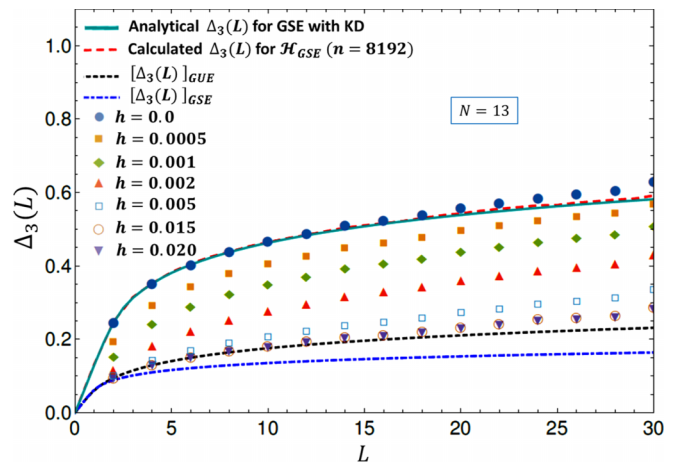


FIG. 13. Calculated spectral rigidity (Δ_3 statistic) of the *consecutive* eigenvalues (keeping all eigenvalues, including the Kramers degenerate ones) for the $N = 13$ spin chain ($\mathcal{M} = 15$) across the GSE-to-GUE crossover with increasing h , and fixed $D = 0.2$ and $\epsilon = 0.6$ (symbols). To compare their extent of agreement with RMT predictions, the analytical expression for the Δ_3 statistic of the non-standard GSE using the consecutive eigenvalues is plotted (cyan line) for a very small value of the crossover parameter (see Appendix D). For comparison, here we also plot the Δ_3 statistic of the RMT matrix model \mathcal{H}_{GSE} ($n = 8192$ and $\mathcal{M} = 10$) (broken lines). One should note that the nonstandard *diluted* GSE plot (red broken line) lies above the standard GUE plot (black broken line), indicating lower correlation or level repulsion on the average. The standard GSE result (blue broken line) is also plotted for comparison, and indeed lies below the standard GUE, confirming a stronger correlation, as expected.

at $h = 0.2$, but coincides with the $[\Sigma^2(L)]_{\text{GUE}}$ only till the interval length $L \sim 4$. Comparing this with the lower value of the NNSD crossover point, $h = 0.15$, we conclude that a relatively higher symmetry-breaking field is required, in this case, to achieve the crossover in the long-range eigenvalue correlation studies.

In Sec. V A, we have studied the short-range GSE-to-GUE (see Table III) crossovers for both the cases where the KD was removed and retained in the eigenvalue spectrum. Here, we study the Δ_3 statistic and the number variance of the spin-chain model H for the GSE-to-GUE crossover, in the Figs. 13 and 14, respectively, by considering the *consecutive* eigenvalues (i.e., retaining all eigenvalues including the Kramers degenerate ones). The analytical form of the Δ_3 statistic as well as that of Σ^2 statistic can be obtained from the two-level cluster function for the GSE-to-GUE crossover [70]; see Appendix D. The GSE limit of this crossover is of special interest due to the consideration of Kramers degenerate eigenvalues. For this limit, we also show the results using the RMT matrix model \mathcal{H}_{GSE} having a dimension $n = 8192$ (similar to our physical $N = 13$ spin-chain model), and calculate the long-range statistics of this model for comparing with that of the physical spin model. In Fig. 13, we observe that $\Delta_3(L)$ plot based on the analytical result for a very small value of the crossover parameter (see Appendix D) agrees very well with the numerical $\Delta_3(L)$ plot for \mathcal{H}_{GSE} , in the GSE limit. Furthermore, for $h = 0.0$, the Δ_3 statistic of H follows the RMT $\Delta_3(L)$ till a large $L \sim 20$. We notice that this

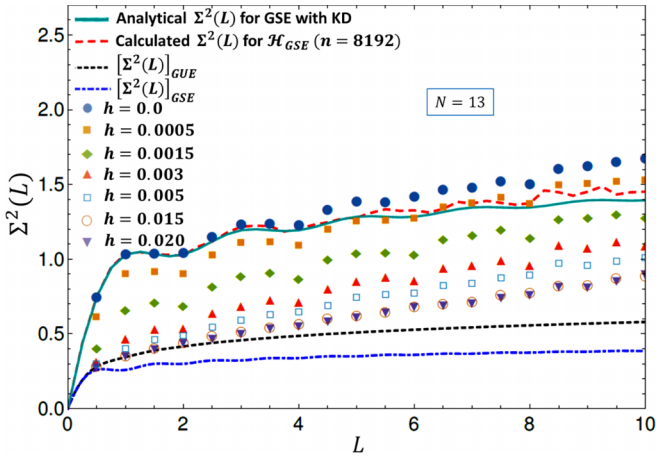


FIG. 14. Number variance (Σ^2 statistic) of the *consecutive* eigenvalues for the $N = 13$ spin-chain system ($\mathcal{M} = 15$), it shows the GSE-to-GUE crossover with increasing h , and fixed $D = 0.2$ and $\epsilon = 0.6$ (symbols). To compare their extent of agreement with RMT predictions, the analytical expression for the Σ^2 statistic of the nonstandard GSE using the consecutive eigenvalues is plotted (cyan line) for a very small value of the crossover parameter (see Appendix D). For comparison, here we plot the $\Sigma^2(L)$ statistic from the RMT matrix model \mathcal{H}_{GSE} ($n = 8192$ and $\mathcal{M} = 15$) (broken lines). One should note that the nonstandard *diluted* GSE plot (red broken line) lies above the standard GUE plot (black broken line), indicating lower correlation or level repulsion on the average. The standard GSE result (blue broken line) is also plotted for comparison, and indeed lies below the standard GUE, confirming a stronger correlation, as expected.

Δ_3 statistic of the *nonstandard* GSE, obtained by retaining all Kramers degeneracies, is always higher in value than the standard GUE class statistics ($[\Delta_3(L)]_{\text{GUE}}$), implying that it is *less correlated* than the GUE on the average. This is contrary to the standard GSE result (after removing the KD by hand), $[\Delta_3(L)]_{\text{GSE}}$, plotted for reference, which is *more correlated* than the standard GUE class (always lower in value). This is a rather interesting result, and may be understood along the lines that retaining all Kramers doublets (no level repulsion between Kramers doublets) amounts to reducing the average correlation or level repulsion compared to the standard GSE case. So it may be looked upon as a *diluted* GSE limit. At the GUE (NNSD) limit, obtained at about $h = 0.015$, the calculated spectral rigidity from the physical model follows the analytical result $[\Delta_3(L)]_{\text{GUE}}$ till about $L \sim 12$ and any further increase in h ($= 0.02$) does not display a better agreement. So, in this study, the limiting case $h = 0.015$ can be designated as a *global* crossover point. In Fig. 14, we observe that, at GSE limit, the calculated $\Sigma^2(L)$ of the spin-chain model, follows the oscillating numerical plot of the RMT analytical as well as the matrix model \mathcal{H}_{GSE} up to $L \sim 4$. This again corresponds to the *diluted* GSE limit, as discussed above, and is *less correlated* compared to the standard GUE limit. On the other hand, just as in the Δ_3 case, the plot for the standard GSE (blue broken lines) is *more correlated* and lies below the standard GUE plot. Beyond $h = 0.005$, the oscillations in the $\Sigma^2(L)$ statistic reduce significantly as we increase h . The calculated $\Sigma^2(L)$ for the physical system at the GUE limit ($h = 0.015$ and 0.02) follows the analytical form of the

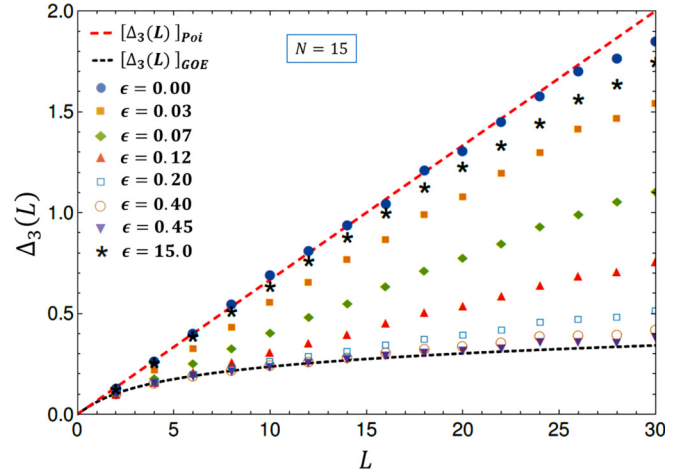


FIG. 15. Spectral rigidity (Δ_3 statistic) for the $N = 15$ spin chain ($\mathcal{M} = 15$) across the Poissonian-to-GOE crossover with increasing ϵ , and fixed $D = 0.2$ (symbols). It also shows the Δ_3 statistic in the many-body localized limit, brought about by the large disorder ($\epsilon = 15.0$) (black asterisks), which is again expected to follow the Poissonian result approximately (red broken line). The GOE limit exact result is also plotted (black broken line) to show the extent of agreement with the physical spin system.

GUE class $[\Sigma^2(L)]_{\text{GUE}}$ only till $L \sim 2$. The standard GSE result (after removing the KD by hand) for the $\Sigma^2(L)$ statistic $[\Sigma^2(L)]_{\text{GSE}}$ is also plotted in Fig. 14, and is consistent with its more correlated nature compared to $[\Sigma^2(L)]_{\text{GUE}}$. Both studies (Δ_3 and Σ^2 statistics) show that all the intermediate cases of the GSE-to-GUE crossovers tend to follow trends that lie between the two limiting cases, resulting in a smooth and continuous transition between the two limits.

Next, we investigate the long-range correlation studies of the reentrant Poissonian-GOE-Poissonian crossover (see Table III) for the spin-chain model H_1 with $N = 15$ lattice sites. While the *ordered* limit for $\epsilon = 0.0$ is the integrable 1D Heisenberg model, the *highly disordered* ($\epsilon = 15.0$) limit includes a very large Ising anisotropy that completely suppresses the quantum fluctuations from the Heisenberg term and results in a many-body localized state that spans only a few relevant basis states. This again is expected to follow the Poissonian distribution [28]. Due to a low dimension of the $S^z = 1/2$ subspace in this case, where the total S^z is conserved, we discarded the $N = 13$ system in favor of the $N = 15$ system, for the long-range correlation calculations of the Poissonian-to-GOE crossover. The corresponding $\Delta_3(L)$ statistic is plotted in Fig. 15 and the $\Sigma^2(L)$ statistic is plotted in Fig. 16. Just as we encountered in the Poissonian-to-GSE-to-Poissonian reentrant crossover (Fig. 1), the two Poissonian limits, $\epsilon = 0.0$ and $\epsilon = 15.0$, coincide with the ideal Poissonian result $[\Delta_3(L)]_{\text{Poi}}$ ($[\Sigma^2(L)]_{\text{Poi}}$) (broken red line) till up to $L \sim 24$ and 8 ($L \sim 2$ and 1), respectively. Again both the *ordered* ($\epsilon = 0$) and the *highly disordered* ($\epsilon = 15.0$) limits tend to agree with the ideal Poissonian prediction till a finite L value, but it seems that the *disordered/localized* Poissonian limit starts to deviate sooner (for a lower L) than the *ordered* Poissonian limit from the ideal Poissonian result for both the Δ_3 and the Σ^2 statistics. The long-range spectral correlations again seem to capture the subtle differences between the two

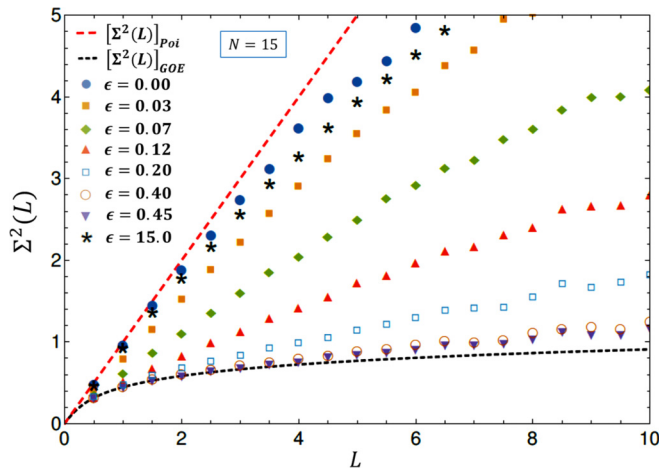


FIG. 16. Number variance (Σ^2 statistic) for the $N = 15$ spin chain ($\mathcal{M} = 15$) across the Poissonian-to-GOE crossover with increasing ϵ , and fixed $D = 0.2$ (symbols). It also shows the Σ^2 statistic for the many-body localized phase, brought about by the large disorder ($\epsilon = 15.0$) (black asterisks), which is again expected to follow the Poissonian result approximately (red broken line). The GOE limit exact result is also plotted (black broken line) to show the extent of agreement with the physical spin system.

Poissonian regimes, that the short-range correlations fail to capture [see Figs. 8(d)–8(f)].

At GOE limit, $\Delta_3(L)$ statistic obeys $[\Delta_3(L)]_{\text{GOE}}$ till $L \sim 16$ for $\epsilon = 0.4$, at which we observed NNSD. If we increase ϵ to 0.45, we do notice improvement in agreement with the standard GOE result, up to till $L \sim 28$. At $\epsilon = 0.45$, the $\Sigma^2(L)$ statistic follow the $[\Sigma^2(L)]_{\text{GOE}}$, only up to an eigenvalue interval $L \sim 5$, and even an increased ϵ does not perform any better.

So, in some cases, we encountered that relatively strong symmetry-breaking interactions are required to achieve a *global* RMT crossover compared to the corresponding *local* crossover. However, in the majority of cases, the long-range fluctuations of physical systems deviate from the standard RMT results after a certain L value, despite perfectly following the short-range NNSD results. We conclude that our physical system is “sufficiently random” for correlations amongst neighboring eigenvalues, but in many cases fail to fully follow the RMT results for correlations amongst distant eigenvalues. Large L deviations in long-range studies suggest a possible breakdown of universality in the level fluctuations of a physical system, implying that spin models are not as correlated as random matrices. Furthermore, for the spin-chain system, while quantifying the same level of long-range correlation, the Σ^2 statistic deviates from the standard RMT results at a much faster rate than the Δ_3 statistic. This could be due to the fact that the Δ_3 statistic is an integral transform of the number variance [see Eq. (D7) of Appendix D] resulting in an agreement with the spin-system results till a much larger value of L [44,72].

VI. CONCLUSIONS

In this paper, we have studied the spectral correlation properties of an interacting quantum spin-chain system with various competing terms, including a coupling to an external

stochastic magnetic field. By tuning the relative amplitudes of these terms, we can alter the unitary and antiunitary symmetries associated with the Hamiltonian. This, in turn, enables us to realize spectral crossovers amongst various Poissonian and Wigner-Dyson classes (GOE, GUE, GSE) of random matrix theory. To quantify these spectral crossovers, we have employed both short-range and long-range random matrix observables, viz., the nearest-neighbor-spacing distribution for the former case, and spectral rigidity and number variance for the latter. The key findings from our extensive study are listed below for both short-range and long-range statistics.

Short-range statistics:

(i) The short-range statistic, NNSD, in all the crossovers, viz., Poissonian-to-GSE, Poissonian-to-GUE, GSE-to-GUE, and Poissonian-to-GOE, exhibit extremely good agreement with the RMT predictions in the two extremes of the crossovers and hence establishes the universality of local spectral fluctuations for our spin-chain system. Moreover, in the intermediate regime, it nicely captures the gradual change in the level-repulsion behavior.

(ii) A crucial aspect of our exploration pertaining to the GSE-to-GUE crossover is retention of the Kramers doubly degenerate eigenvalues in the GSE limit, which is typically not done while studying the spectral correlation properties of the GSE class. In this limit, the NNSD exhibits a Dirac-delta peak at the origin along with a broad Wigner-Dyson like hump at a finite spacing value of s . For this case, we have also presented an analytical expression for the NNSD of the renormalized GSE class, which matches well with the observations from the RMT matrix model and the spin-chain system.

(iii) Within the GSE-to-GUE crossover, as the Kramers degeneracy is lifted via the breaking of an appropriate antiunitary symmetry, an interesting double-peak structure is observed in the NNSD, which eventually turns into a single-peak Wigner-Dyson curve of the standard GUE NNSD. The evolution of the eigenspectra undergoing the GSE-to-GUE transition is presented through the study of the marginal spectral densities (MSD) and the densities of states (DOS) for both the spin model as well as the relevant RMT crossover matrix model.

(iv) The reentrant Poissonian-to-GOE-to-Poissonian nonrandom(\rightarrow chaotic \rightarrow localized) crossover is observed by gradually increasing the disorder in the system via an increase in the random Ising coupling ϵ . The appearance of the Poissonian statistics in the two extreme limits around the Wigner-Dyson distribution, one delocalized and the other localized in the many-body Slater basis, is successfully demonstrated in this study.

Long-range statistics:

(i) The long-range correlation statistics match with RMT predictions in the extreme limits up to a certain spectral length interval L and deviate for larger L values, which indicates that the spectral correlations for the physical spin system are indeed different from RMT long-range correlations as one examines intervals of larger lengths. This may, in turn, be related to the relatively short spatial range of the physical interactions in our spin models.

(ii) In the GSE limit of the GSE-to-GUE crossover, the consequence of keeping all the eigenvalues (including the

Kramers doublets) is that a less correlated behavior, viz., higher values of $\Delta_3(L)$ and $\Sigma^2(L)$ compared to the standard GSE, and also the standard GUE, is observed for our spin system. This seems to nicely agree with similar trends shown by the analytical RMT results for the standard GUE and GSE extremes as well as the GSE limit with Kramers degeneracy (referred to as the *diluted* GSE limit) as derived in Appendix D, in that the *diluted* GSE plots lie not only above the standard GSE, but also above the plots for the standard GUE, for both Δ_3 and Σ^2 , indicating lower correlation.

(iii) Another key finding of our study is that the integrable Poissonian limit, which is realized in the two extreme regimes, one in the absence and the other in the presence of many-body localization, while not being distinguishable at the level of the NNSD, does show a discernible behavior with respect to the long-range correlations. The latter, therefore, can serve as indicators to distinguish between these two regimes.

From the above, it is evident that by tuning the various competing terms in the spin-chain Hamiltonian, which control various unitary and antiunitary symmetries, a rich variety of crossovers is observed in the short-range as well as in the long-range statistics of the eigenvalues. One particularly interesting aspect of our study has been examining the consequences of retaining the Kramers degenerate eigenvalues in the GSE limit. It would be of interest to explore this facet in other many-body physical systems as well. One would also like to go beyond the eigenvalues and quantify the behavior of eigenvectors in such symmetry crossovers in physical systems using statistics such as inverse participation ratio, generalized information entropies and multifractal dimensions. Some of these investigations are already under way.

ACKNOWLEDGMENTS

D.K. and S.S.G. acknowledge the Science and Engineering Research Board (SERB), Department of Science and Technology (DST), Government of India, for financial support via Project No. ECR/2016/002054. S.K. acknowledges financial support provided by SERB, DST, Government of India, via Project No. CRG/2022/001751. We would like to dedicate this article to the memory of Prof. Akhilesh Pandey, a doyen in the field of Random Matrix Theory.

APPENDIX A: SIMPLIFICATION OF THE DM TERM

This Appendix presents a simplification of the DM interaction term (H_{DM}) mentioned in Eq. (1). We have

$$H_{DM} = \sum_{j=1}^{N-1} \mathbf{D} \cdot [\mathbf{S}_j \times \mathbf{S}_{j+1}]. \quad (\text{A1})$$

After expanding the term $\mathbf{D} \cdot [\mathbf{S}_j \times \mathbf{S}_{j+1}]$ in terms of the spin components (S^x, S^y, S^z) we get

$$\begin{aligned} \mathbf{D} \cdot [\mathbf{S}_j \times \mathbf{S}_{j+1}] &= D_x (S_j^y S_{j+1}^z - S_j^z S_{j+1}^y) \\ &+ D_y (-S_j^x S_{j+1}^z + S_j^z S_{j+1}^x) + D_z (S_j^x S_{j+1}^y - S_j^y S_{j+1}^x). \end{aligned} \quad (\text{A2})$$

Now, in terms of the site spin *raising* (S_j^+) and *lowering* (S_j^-) (or spin *ladder*) operators

$$S_j^x = \frac{1}{2}(S_j^+ + S_j^-), \quad S_j^y = \frac{1}{2i}(S_j^+ - S_j^-), \quad (\text{A3})$$

we have after simplification

$$\begin{aligned} \mathbf{D} \cdot [\mathbf{S}_j \times \mathbf{S}_{j+1}] &= \frac{iD_x}{2} (-S_j^+ S_{j+1}^z + S_j^- S_{j+1}^z + S_j^z S_{j+1}^+ - S_j^z S_{j+1}^-) \\ &+ \frac{D_y}{2} (-S_j^+ S_{j+1}^z - S_j^- S_{j+1}^z + S_j^z S_{j+1}^+ + S_j^z S_{j+1}^-) \\ &+ \frac{iD_z}{2} (S_j^+ S_{j+1}^- - S_j^- S_{j+1}^+). \end{aligned} \quad (\text{A4})$$

The terms, which involve a single spin ladder operator, like $S_j^+ S_{j+1}^z$ ($S_j^- S_{j+1}^z$), increase (decrease) the total S^z of the system by 1. On the other hand, the two-site terms like $S_j^+ S_{j+1}^-$ and $S_j^- S_{j+1}^+$, conserve total S^z . The terms with two similar spin ladder operators (like $S_j^+ S_{j+1}^+$ and $S_j^- S_{j+1}^-$) cancel out during the simplification. From Eq. (A4), we observe that the spin operators associated with the D_x and D_y terms, connect nearest-neighbor S^z sectors, but the spin operators associated with the D_z term do not connect different S^z sectors. Thus, for nonzero D_x and/or D_y , we cannot carry out calculations within a fixed S^z sector.

APPENDIX B: CONSERVATION OF THE SPIN COMPONENT ALONG THE DIRECTION OF THE VECTOR COUPLING UNDER THE DM INTERACTION TERM

In this Appendix, we show that H_{DM} commutes with $\mathbf{S} \cdot \hat{D}$, resulting in H_{DM} having cylindrical symmetry only about the direction of \hat{D} . We consider two spins, \mathbf{S}_1 and \mathbf{S}_2 , for which $H_{DM} = \mathbf{D} \cdot [\mathbf{S}_1 \times \mathbf{S}_2]$ and $\mathbf{S} = \mathbf{S}_1 + \mathbf{S}_2$. Using a tensorial notation along with the summation convention, we write the vector $\mathbf{D} = D_\alpha \hat{e}_\alpha$, where \hat{e}_α is the unit vector along the three Cartesian axes ($\alpha = 1, 2, 3$ corresponds to the x, y, z axes, respectively). The unit vector along \mathbf{D} is $\hat{D} = d_\alpha \hat{e}_\alpha$, where $d_\alpha = D_\alpha / D$ ($d_\alpha d_\alpha = 1$).

Now, we have

$$[H_{DM}, \mathbf{S} \cdot \hat{D}] = H_{DM}(\mathbf{S} \cdot \hat{D}) - (\mathbf{S} \cdot \hat{D})H_{DM}. \quad (\text{B1})$$

The first term in the right-hand side can be written as

$$\begin{aligned} H_{DM}(\mathbf{S} \cdot \hat{D}) &= (\varepsilon_{\alpha\beta\gamma} D_\alpha S_{1\beta} S_{2\gamma})(S_{1\mu} + S_{2\mu})d_\mu \\ &= d_\mu (\varepsilon_{\alpha\beta\gamma} D_\alpha S_{1\beta} S_{2\gamma} S_{1\mu} + \varepsilon_{\alpha\beta\gamma} D_\alpha S_{1\beta} S_{2\gamma} S_{2\mu}) \\ &= d_\mu (\varepsilon_{\alpha\beta\gamma} D_\alpha S_{1\beta} S_{1\mu} S_{2\gamma} + i\varepsilon_{\alpha\beta\gamma} \varepsilon_{\gamma\mu\eta} D_\alpha S_{1\beta} S_{2\eta} \\ &\quad + \varepsilon_{\alpha\beta\gamma} D_\alpha S_{1\beta} S_{2\mu} S_{2\gamma}), \end{aligned} \quad (\text{B2})$$

where in the last step we have used the fact that, spin operators from different sites commute and the commutation relation for the same-site spin operators is $[S_{2\gamma}, S_{2\mu}] = i\varepsilon_{\gamma\mu\eta} S_{2\eta}$, which may be combined into $[S_{p\gamma}, S_{q\mu}] = i\delta_{pq} \varepsilon_{\gamma\mu\eta} S_{p\eta}$. Similarly,

we get the further simplified form as

$$\begin{aligned} H_{\text{DM}}(\mathbf{S} \cdot \hat{D}) &= d_\mu (i\varepsilon_{\alpha\beta\gamma}\varepsilon_{\beta\mu\eta}D_\alpha S_{1\eta}S_{2\gamma} + S_{1\mu}\varepsilon_{\alpha\beta\gamma}D_\alpha S_{1\beta}S_{2\gamma} \\ &\quad + i\varepsilon_{\alpha\beta\gamma}\varepsilon_{\gamma\mu\eta}D_\alpha S_{1\beta}S_{2\eta} + S_{2\mu}\varepsilon_{\alpha\beta\gamma}D_\alpha S_{1\beta}S_{2\gamma}). \end{aligned} \quad (\text{B3})$$

Now, we use the identity $\varepsilon_{ijk}\varepsilon_{imn} = \delta_{jm}\delta_{kn} - \delta_{jn}\delta_{km}$, and the antisymmetry of the Levi-Civita tensor, whence the *first* term of Eq. (B3) becomes

$$\begin{aligned} i\varepsilon_{\alpha\beta\gamma}\varepsilon_{\beta\mu\eta}D_\alpha S_{1\eta}S_{2\gamma}d_\mu &= -i\varepsilon_{\beta\alpha\gamma}\varepsilon_{\beta\mu\eta}D_\alpha S_{1\eta}S_{2\gamma}d_\mu \\ &= -i(D_\mu d_\mu)(S_{1\gamma}S_{2\gamma}) + i(D_\alpha S_{1\alpha})(S_{2\mu}d_\mu) \\ &= -i(\hat{D} \cdot \mathbf{D})(\mathbf{S}_1 \cdot \mathbf{S}_2) + i(\mathbf{S}_1 \cdot \mathbf{D})(\mathbf{S}_2 \cdot \hat{D}) \\ &= -iD[\mathbf{S}_1 \cdot \mathbf{S}_2 - (\mathbf{S}_1 \cdot \hat{D})(\mathbf{S}_2 \cdot \hat{D})]. \end{aligned} \quad (\text{B4})$$

Similarly, the *third* term of Eq. (B3) becomes

$$i\varepsilon_{\alpha\beta\gamma}\varepsilon_{\gamma\mu\eta}D_\alpha S_{1\beta}S_{2\eta}d_\mu = iD[\mathbf{S}_1 \cdot \mathbf{S}_2 - (\mathbf{S}_1 \cdot \hat{D})(\mathbf{S}_2 \cdot \hat{D})]. \quad (\text{B5})$$

From the Eqs. (B4) and (B5), we see that the *first* and the *third* terms of Eq. (B3) cancel out each other. From the *second* and the *fourth* terms of Eq. (B3) we get

$$\begin{aligned} H_{\text{DM}}(\mathbf{S} \cdot \hat{D}) &= (S_{1\mu}d_\mu)(\varepsilon_{\alpha\beta\gamma}D_\alpha S_{1\beta}S_{2\gamma}) \\ &\quad + (S_{2\mu}d_\mu)(\varepsilon_{\alpha\beta\gamma}D_\alpha S_{1\beta}S_{2\gamma}) \\ &= (S_{1\mu} + S_{2\mu})d_\mu(\varepsilon_{\alpha\beta\gamma}D_\alpha S_{1\beta}S_{2\gamma}) \\ &= (\mathbf{S} \cdot \hat{D})H_{\text{DM}}. \end{aligned} \quad (\text{B6})$$

So we get $[H_{\text{DM}}, \mathbf{S} \cdot \hat{D}] = 0$ that establishes the said conservation law and resultant cylindrical symmetry about the \mathbf{D} axis.

APPENDIX C: CALCULATION OF THE NNSD OF THE GSE CLASS WITH KD

Consider the ordered spectrum with Kramers degeneracy having n levels $\varepsilon_1 = \varepsilon_2 < \varepsilon_3 = \varepsilon_4 < \dots < \varepsilon_{n-1} = \varepsilon_n$, where n is even. In finding the nearest-neighbor spacings, we have $(n-1)$ level-spacings in all. The degenerate pairs will lead to $\frac{n}{2}$ zero-level spacings, while the nondegenerate ones will lead to $(\frac{n}{2} - 1)$ nonzero (positive) level spacings. Denoting the unnormalized level spacings by the variable x , the zero spacings give rise to a Dirac delta $[\delta(x)]$ peak at $x = 0$, and the distribution of nonzero part is expected to follow the standard NNSD of GSE $P_{\text{GSE}}(x)$. Including both these contributions, the NNSD in the case where the Kramers degeneracy is retained, should be given by a function of the form

$$f^n(x) = f_{\text{GSE}}^n(x) + f_0^n(x) = \mu P_{\text{GSE}}(x) + \nu \delta(x), \quad (\text{C1})$$

where μ and ν are determined by making use of the fractional contributions from the two types of spacings (*zero* and *finite*) to the overall normalized distribution $f^n(x)$, also using the individual normalization properties of $P_{\text{GSE}}(x)$ and $\delta(x)$, as discussed below. The normalization condition demands that the integrated weight of $f^n(x)$ should be 1. So, the fractional

weight of the nonzero spacings becomes

$$\int_0^\infty f_{\text{GSE}}^n(x)dx = \frac{(\frac{n}{2} - 1)}{(n-1)} = \frac{1}{2} \left(\frac{n-2}{n-1} \right), \quad (\text{C2})$$

and of the zero spacings becomes

$$\int_0^\infty f_0^n(x)dx = \frac{\frac{n}{2}}{(n-1)} = \frac{1}{2} \left(\frac{n}{n-1} \right). \quad (\text{C3})$$

From Eq. (C1) and Eq. (C2) we get

$$\mu \int_0^\infty P_{\text{GSE}}(x)dx = \frac{1}{2} \left(\frac{n-2}{n-1} \right), \quad (\text{C4})$$

and using the normalization condition $\int_0^\infty P_{\text{GSE}}(x)dx = 1$, we find $\mu = \frac{1}{2} \left(\frac{n-2}{n-1} \right)$. Again, from Eq. (C1) and Eq. (C3) we have

$$\nu \int_0^\infty \delta(x)dx = \frac{1}{2} \left(\frac{n}{n-1} \right). \quad (\text{C5})$$

Using the definition of the Dirac delta function $\int_0^\infty \delta(x)dx := \frac{1}{2}$, we have $\nu = \frac{n}{n-1}$, and $f^n(x)$ now becomes

$$f^n(x) = \frac{1}{2} \left(\frac{n-2}{n-1} \right) P_{\text{GSE}}(x) + \left(\frac{n}{n-1} \right) \delta(x). \quad (\text{C6})$$

We need to now calculate the average spacings for the distribution $f^n(x)$. We consider

$$\begin{aligned} \mathcal{D} &= \int_0^\infty f^n(x)dx \\ &= \frac{1}{2} \left(\frac{n-2}{n-1} \right) \int_0^\infty x P_{\text{GSE}}(x) + \left(\frac{n}{n-1} \right) \int_0^\infty x \delta(x) \\ &= \frac{1}{2} \left(\frac{n-2}{n-1} \right), \end{aligned} \quad (\text{C7})$$

here we have used the unfolding condition $\int_0^\infty x P_{\text{GSE}}(x) = 1$ and the relation for the Dirac delta function $\int_0^\infty x \delta(x) := 0$. In order to again make the average spacing equal to 1, we define the normalized variable $s = x/\mathcal{D}$, and rewrite the distribution in terms of this new variable. Considering the Jacobian of transformation $|dx/ds| = \frac{1}{2} \left(\frac{n-2}{n-1} \right)$, we get the rescaled distribution as

$$\begin{aligned} \mathcal{P}_{\text{GSE}}^n(s) &= \frac{1}{2} \left[\frac{n-2}{n-1} \right] \left\{ f^n \left(\frac{1}{2} \left[\frac{n-2}{n-1} \right] s \right) \right\} \\ &= \frac{1}{2} \left[\frac{n-2}{n-1} \right] \left\{ \frac{1}{2} \left[\frac{n-2}{n-1} \right] P_{\text{GSE}} \left(\frac{1}{2} \left[\frac{n-2}{n-1} \right] s \right) \right\} \\ &\quad + \frac{1}{2} \left[\frac{n-2}{n-1} \right] \left\{ \left[\frac{n}{n-1} \right] \delta \left(\frac{1}{2} \left[\frac{n-2}{n-1} \right] s \right) \right\}. \end{aligned} \quad (\text{C8})$$

Using the standard analytical expression for $P_{\text{GSE}}(s)$, based on the Wigner surmise, and the scaling property of the Dirac delta function $\delta(ks) = \delta(s)/|k|$, we simplify the Eq. (C8) and get the modified analytical form of the NNSD, for the GSE class $[\mathcal{P}_{\text{GSE}}^n(s)]$, where the Kramers degeneracy is not removed

from the eigenspectrum. For dimension n , it is presented as

$$\mathcal{P}_{\text{GSE}}^n(s) = \left[\frac{2^{12}}{3^6 \pi^3} \left(\frac{n-2}{n-1} \right)^6 s^4 \right] \exp \left[-\frac{16}{9\pi} \left(\frac{n-2}{n-1} \right)^2 s^2 \right] + \left(\frac{n}{n-1} \right) \delta(s). \quad (\text{C9})$$

For a large n (like for our $n = 8192$ calculation, but not the $n = 4$ calculation), Eq. (C9) assumes the asymptotic form

$$\mathcal{P}_{\text{GSE}}(s) = \left(\frac{2^{12}}{3^6 \pi^3} s^4 \right) \exp \left(-\frac{16}{9\pi} s^2 \right) + \delta(s). \quad (\text{C10})$$

APPENDIX D: FULL INTEGRAL EXPRESSIONS FOR $\Delta_3(L)$ AND $\Sigma^2(L)$

In this Appendix, we present the full integral expressions of the $\Delta_3(L)$ and $\Sigma^2(L)$ statistics in terms of the two-level *cluster functions* [39]. The correlation characteristics of a single cluster of n levels are described by the *cluster function*, which is separate from the lower order correlations [39]. It vanishes when any one (or more) of the level separations ($|\tilde{\epsilon}_i - \tilde{\epsilon}_j|$) increases relative to the local mean level spacing (which is unity for our case). The two-level *cluster functions* for various cases are listed below [39],

$$Y_{\text{Poi}}(r) = 0, \quad (\text{D1})$$

$$Y_{\text{GOE}}(r) = \left(\frac{\sin(\pi r)}{\pi r} \right)^2 + \left(\frac{\cos(\pi r)}{r} - \frac{\sin(\pi r)}{\pi r^2} \right) \left(\frac{1}{2} - \frac{\text{Si}(\pi r)}{\pi} \right), \quad (\text{D2})$$

$$Y_{\text{GUE}}(r) = \left(\frac{\sin(\pi r)}{\pi r} \right)^2, \quad (\text{D3})$$

$$Y_{\text{GSE}}(r) = \left(\frac{\sin(2\pi r)}{2\pi r} \right)^2 - \left(\frac{\cos(2\pi r)}{r} - \frac{\sin(2\pi r)}{2\pi r^2} \right) \left(\frac{\text{Si}(2\pi r)}{2\pi} \right), \quad (\text{D4})$$

where $r = |\tilde{\epsilon}_1 - \tilde{\epsilon}_2|$ and $\text{Si}(z) = \int_0^z \sin(t)/t dt$ is the standard sine integral.

The full integral expressions of the averaged Δ_3 statistic and Σ^2 statistic are given by [39]

$$\Delta_3(L) = \frac{L}{15} - \frac{1}{15L^4} \int_0^L (L-r)^3 (2L^2 - 9Lr - 3r^2) Y(r) dr, \quad (\text{D5})$$

and

$$\Sigma^2(L) = L - 2 \int_0^L (L-r) Y(r) dr. \quad (\text{D6})$$

It is also known that $\Delta_3(L)$ is an integral transform of $\Sigma^2(L)$ [44,68,72],

$$\Delta_3(L) = \frac{2}{L^4} \int_0^L (L^3 - 2L^2 r + r^3) \Sigma^2(r) dr. \quad (\text{D7})$$

The above integrals for $\Delta_3(L)$ and $\Sigma^2(L)$ for the Wigner-Dyson ensembles can be performed in terms of the sine and cosine integrals, but are lengthy. In Sec. VB, we used numerical evaluations of the aforementioned integral formulas for the specific ranges of L , and presented the results in the relevant Figs. 9–16.

For the GSE-to-GUE crossover, the exact as well as asymptotic expressions for correlation functions and cluster functions are known [69]. The evaluation of spectral rigidity and number variance requires the two-level cluster function for the unfolded eigenvalues, which is given as [69,76]

$$Y_{\text{GSE-GUE}}(\lambda, r) = \left(\frac{\sin(\pi r)}{\pi r} \right)^2 - I(\lambda, r) K(\lambda, r), \quad (\text{D8})$$

where

$$I(\lambda, r) = -\frac{1}{\pi} \int_0^\pi \frac{\sin(kr)}{k} e^{2\lambda^2 k^2} dk, \quad (\text{D9})$$

$$K(\lambda, r) = -\frac{1}{\pi} \int_\pi^\infty k \sin(kr) e^{-2\lambda^2 k^2} dk. \quad (\text{D10})$$

The parameter $\lambda \sim \sqrt{n}\alpha$ in the above expressions is the rescaled-crossover parameter. We use the above λ -dependent cluster function expression in Eqs. (D5) and (D6) to obtain the spectral rigidity and number variance. The GSE limit is obtained for $\lambda \rightarrow 0$, whereas the GUE limit is achieved for $\lambda \rightarrow \infty$, for which the product $I(\lambda, r)K(\lambda, r)$ goes to zero. It should be noted that the crossover is almost complete for $\lambda \sim 1$, i.e., $\alpha \sim 1/\sqrt{n}$.

The above integrals need to be numerically evaluated to obtain the number variance and spectral rigidity in the GSE-to-GUE crossover. The limit $\lambda \rightarrow 0$ poses difficulty in numerical evaluation as $I(\lambda, r)$ and $K(\lambda, r)$ approach $-\text{sgn}(r)/2$ and $\delta(r)/r$, respectively; the latter signifying the Kramers degeneracy. Therefore, we perform the evaluation of the above integrals for nonzero, but small λ values using very high precision. For instance, for the GSE curves in Figs. 12 and 13, we have used $\lambda = 1/600$.

[1] J. Hubbard, *J. Proc. R. Soc. A* **276**, 237 (1963).

[2] P. Fazekas, *Lecture Notes on Electron Correlation and Magnetism* (World Scientific, Singapore, 1999).

[3] E. H. Lieb, *The Hubbard Model* (Springer, New York, 1995).

[4] G. D. Mahan, *Many-Particle Physics* (Springer, New York, 2000).

[5] F. H. L. Essler, H. Frahm, F. Göhmann, A. Klümper, and V. E. Korepin, *The One-Dimensional Hubbard Model* (Cambridge University Press, Cambridge, 2005).

[6] W. Heisenberg, *Z. Phys.* **49**, 619 (1928).

[7] W. Lenz, *Z. Phys.* **21**, 613 (1920).

[8] E. Ising, *Z. Phys.* **31**, 253 (1925).

[9] H. Bethe, *Z. Phys.* **71**, 205 (1931).

[10] R. J. Baxter, *Ann. Phys.* **70**, 193 (1972).

[11] E. Lieb, T. Schultz, and D. Mattis, *Ann. Phys.* **16**, 407 (1961).

[12] T. Moriya, *Phys. Rev. Lett.* **4**, 228 (1960).

[13] T. Moriya, *Phys. Rev.* **120**, 91 (1960).

- [14] I. Dzyaloshinsky, *J. Phys. Chem. Solids* **4**, 241 (1958).
- [15] X. G. Wen, F. Wilczek, and A. Zee, *Phys. Rev. B* **39**, 11413 (1989).
- [16] D. S. Rokhsar, *Phys. Rev. Lett.* **65**, 1506 (1990).
- [17] J. K. Freericks, L. M. Falicov, and D. S. Rokhsar, *Phys. Rev. B* **44**, 1458 (1991).
- [18] D. Sen and R. Chitra, *Phys. Rev. B* **51**, 1922 (1995).
- [19] P. W. Anderson, *Phys. Rev.* **124**, 41 (1961).
- [20] E. Abrahams, P. W. Anderson, D. C. Licciardello, and T. V. Ramakrishnan, *Phys. Rev. Lett.* **42**, 673 (1979).
- [21] P. W. Anderson, D. J. Thouless, E. Abrahams, and D. S. Fisher, *Phys. Rev. B* **22**, 3519 (1980).
- [22] A. Legendijk, B. v. Tiggelen, and D. S. Wiersma, *Phys. Today* **62**(8), 24 (2009).
- [23] P. A. Lee and T. V. Ramakrishnan, *Rev. Mod. Phys.* **57**, 287 (1985).
- [24] A. L. Efros and B. I. Shklovskii, *J. Phys. C: Solid State Phys.* **8**, L49 (1975).
- [25] R. A. Römer and A. Punnoose, *Phys. Rev. B* **52**, 14809 (1995).
- [26] A. Punnoose and A. M. Finkel'stein, *Science* **310**, 289 (2005).
- [27] A. Punnoose and A. M. Finkel'stein, *Phys. Rev. Lett.* **96**, 057202 (2006).
- [28] D. Kundu, S. Kumar, and S. Sen Gupta, *Phys. Rev. B* **105**, 014205 (2022).
- [29] Y. Avishai, J. Richert, and R. Berkovits, *Phys. Rev. B* **66**, 052416 (2002).
- [30] R. Modak and S. Mukerjee, *New J. Phys.* **16**, 093016 (2014).
- [31] E. P. Wigner, *Proc. Cambridge Philos. Soc.* **47**, 790 (1951).
- [32] E. P. Wigner, *Gathnberg Conference on Neutron Physics by Time-of-Flight* (Oak-Ridge National Laboratory Report No. 2309, US, 1957) p. 59.
- [33] E. P. Wigner, *Statistical Properties of Real Symmetric Matrices with Many Dimensions* (Princeton University Press, Princeton, NJ, 1957) pp. 188–198.
- [34] E. Wigner, *Phys. Rev.* **40**, 749 (1932).
- [35] E. P. Wigner, *Ann. Math.* **62**, 548 (1955).
- [36] E. P. Wigner, *Ann. Math.* **65**, 203 (1957).
- [37] E. P. Wigner, *Ann. Math.* **67**, 325 (1958).
- [38] F. J. Dyson, *J. Math. Phys.* **3**, 140 (1962).
- [39] M. Mehta, *Random Matrices*, Pure and Applied Mathematics (Elsevier Science, Netherlands, 2004).
- [40] M. Mehta, *Nucl. Phys.* **18**, 395 (1960).
- [41] F. Haake, S. Gnutzmann, and M. Kuś, *Quantum Signatures of Chaos*, 4th ed. (Springer, Cham, 2018).
- [42] L. E. Reichl, *The Transition to Chaos: Conservative Classical Systems and Quantum Manifestations* (Springer, New York, 2004).
- [43] L. E. Stöckmann, *Quantum Chaos: An Introduction* (Cambridge University Press, Cambridge, 2007).
- [44] T. Guhr, A. Muller-Groeling, and H. A. Weidenmuller, *Phys. Rep.* **299**, 189 (1998).
- [45] C. W. J. Beenakker, *Rev. Mod. Phys.* **69**, 731 (1997).
- [46] Y. Alhassid, *Rev. Mod. Phys.* **72**, 895 (2000).
- [47] B. I. Shklovskii, B. Shapiro, B. R. Sears, P. Lambrianides, and H. B. Shore, *Phys. Rev. B* **47**, 11487 (1993).
- [48] O. Bohigas, M. J. Giannoni, and C. Schmit, *Phys. Rev. Lett.* **52**, 1 (1984).
- [49] M. V. Berry, M. Tabor, and J. M. Ziman, *Proc. R. Soc. London A* **356**, 375 (1977).
- [50] A. Y. Abul-Magd and M. H. Simbel, *Phys. Rev. E* **60**, 5371 (1999).
- [51] M. Collura, H. Aufderheide, G. Roux, and D. Karevski, *Phys. Rev. A* **86**, 013615 (2012).
- [52] N. Chavda and V. Kota, *Phys. Lett. A* **377**, 3009 (2013).
- [53] S. Iyer, V. Oganessian, G. Refael, and D. A. Huse, *Phys. Rev. B* **87**, 134202 (2013).
- [54] M. S. Santhanam and P. K. Patra, *Phys. Rev. E* **64**, 016102 (2001).
- [55] A. Pandey, S. Puri, and S. Kumar, *Phys. Rev. E* **71**, 066210 (2005).
- [56] S. Jalan and J. N. Bandyopadhyay, *Phys. Rev. E* **76**, 046107 (2007).
- [57] S. M. Abuelenin and A. Y. Abul-Magd, *Procedia Comput. Sci.* **12**, 69 (2012).
- [58] C. L. Bertrand and A. M. García-García, *Phys. Rev. B* **94**, 144201 (2016).
- [59] F. J. Dyson and M. L. Mehta, *J. Math. Phys.* **4**, 701 (1963).
- [60] C. W. J. Beenakker, *Rev. Mod. Phys.* **87**, 1037 (2015).
- [61] R. Hamazaki and M. Ueda, *Phys. Rev. E* **99**, 042116 (2019).
- [62] J. Vahedi, A. Ashouri, and S. Mahdaviifar, *Chaos* **26**, 103106 (2016).
- [63] K. Yosida, *Theory of Magnetism* (Springer, Berlin, 1996).
- [64] A. Gubin and L. F. Santos, *Am. J. Phys.* **80**, 246 (2012).
- [65] J. L. Lebowitz and O. Penrose, *Phys. Today* **26**, 23 (1973).
- [66] O. Penrose, *Rep. Prog. Phys.* **42**, 1937 (1979).
- [67] G. Gallavotti, *Statistical Mechanics: A Short Treatise*, 1st ed. (Springer-Verlag, Berlin, 1999).
- [68] T. A. Brody, J. Flores, J. B. French, P. A. Mello, A. Pandey, and S. S. M. Wong, *Rev. Mod. Phys.* **53**, 385 (1981).
- [69] A. Pandey and M. L. Mehta, *Commun. Math. Phys.* **87**, 449 (1983).
- [70] M. L. Mehta and A. Pandey, *J. Phys. A: Math. Gen.* **16**, 2655 (1983).
- [71] G. Lenz and F. Haake, *Phys. Rev. Lett.* **65**, 2325 (1990).
- [72] M. Vyas and T. H. Seligman, in *Latin-American School of Physics Marcos Moshinsky ELAF2017: Quantum Correlations*, edited by J. A. Seman, R. Paredes, and R. Jáuregui, AIP Conf. Proc. No. 1950 (AIP, New York, 2018), p. 030009.
- [73] S. Kumar and A. Pandey, *Ann. Phys.* **326**, 1877 (2011).
- [74] A. Pandey, *Ann. Phys.* **134**, 110 (1981).
- [75] A. Pandey, *Ann. Phys.* **119**, 170 (1979).
- [76] S. Kumar and A. Pandey, *Phys. Rev. E* **79**, 026211 (2009).